Design Report of the Central Preshower Detector for the DØ Upgrade

M. Adams[a], N. Amos[b], S. Chopra[b], M. Chung[a], K. Del Signore[b], F. Hsieh[b], H. Li[c], D. Lincoln[b], H. Neal[b], E. Neis[b], J. Qian[b], M. Rijssenbeek[c]

[a] *University of Illinois at Chicago, Chicago, Illinois 60607*
[b] *University of Michigan, Ann Arbor, Michigan 48109*
[c] *State University of New York, Stony Brook, New York 11794*

(January 15, 1996)

Abstract

The DØ central preshower detector is designed to improve electron identification and to help restore the electromagnetic energy resolution otherwise degraded by the presence of the solenoid. The cylindrically shaped scintillating detector with axial and stereo views will be installed between the calorimeter and the solenoid. Scintillating light produced by charged particles will be collected by the wavelength-shifting fibers and piped through clear fibers to the visible light photon counters. This report describes the basic geometry, simulation results, cosmic–ray test results of prototype modules, mechanical assembly, monitoring and calibration schemes of the central preshower detector.

Contents

I. INTRODUCTION

The recent discovery [1] of the top quark at Fermilab provided crucial evidence for the validity of the Standard Model, which has survived extensive experimental tests. Despite these successes, there are many compelling questions that the Standard Model alone cannot address. Additional experimental data are required to answer some of the most fundamental questions of nature. Fermilab has the highest energy accelerator in the world. The Tevatron $\bar{p}p$ accelerator provides a unique opportunity for testing the Standard Model and searching for new physics beyond the Standard Model which currently can not be pursued elsewhere.

The DØ detector [2] was constructed to study high mass and high p_T phenomena and the detector has been performing extraordinarily well in the current Tevatron Run I, as is well demonstrated by the top quark discovery and other published physics results. The detector has been, and will remain, one of the two most promising detectors in the world for pursuing high p_T physics in the next decade. With the continued improvement in the Tevatron luminosity and the experience gained in operating the DØ detector and in analyzing data from Run I, the collaboration has proposed to upgrade the detector [3] to insure the fullest exploitation of physics opportunities for the Tevatron Run II expected to begin in 1999. The DØ upgrade is designed to adapt the detector to a higher luminosity, to improve high p_T physics capability by replacing the current non–magnetic tracking system with a high resolution magnetic tracking and vertex determination system. In addition, a preshower detector will be added to aid electron identification and to help restore the electromagnetic energy resolution otherwise degraded by the presence of the solenoid.

Electrons play an indispensible role in high p_T physics at the Tevatron collider. The success of the Tevatron Run II physics program depends on whether the detector can efficiently identify electrons and muons both on–line and off–line with an acceptable background level at high luminosity. Given a limited trigger bandwidth, additional background rejection is needed for lepton triggers at the high luminosity expected from the Tevatron Run II. It is for the purpose of electron identification that the central preshower detector is proposed. The preshower detector will provide an additional means of distinguishing electrons from the background. Furthermore, the energy sampling provided by a preshower detector, installed between the solenoid and the calorimeter, will also help restore electromagnetic energy resolution degraded by the presence of the solenoid.

In the past year or so, our effort has been primarily directed towards the simulation and R&D of the central preshower detector. Indeed, significant progress has been made on those fronts. Based on the experiences gained through the simulation and the R&D effort, we have developed a detailed design of the detector. In this report, we will summarize the results of simulation and the prototype cosmic–ray test. We will also present some design issues such as the basic detector geometry, mechanical assembly, connectors, calibration schemes and the construction schedule of the detector. Presently, the project involves about 12 physicists and students from the University of Michigan, SUNY at Stony Brook and the University of Illinois at Chicago (UIC).

II. THE PROPOSED DETECTOR

The central preshower detector must function as a calorimeter by early energy sampling and as a tracker by providing precision position measurements. These are the two basic requirements on which the following detector is proposed.

A. Overview

Given the compact nature of the DØ detector, space is an issue for any new detector component. The space available for a preshower detector is no exception. There is only a 5.0 cm radial space between the solenoid and the calorimeter. With this limitation and cost consideration, a scintillator based detector becomes the practical choice for the preshower detector. The preshower detector will consist of a tapered lead radiator plus three layers of finely segmented scintillating strips with wavelength–shifting (WLS) fiber readout. Although a design with a 90° stereo angle has been considered, ultimately the choice of a $\sim 20°$ stereo angle was made. In this design, the three layers of strips will be arranged in $z - u - v$ views. The cylindrically shaped detector will be placed directly outside the solenoid and inside the DØ central calorimeter cryostat bore at a radius of about 72 cm. The solenoid consists of about one radiation length (X_0) of material at normal incidence. The lead radiator will be tapered along the beam direction so the coil plus lead yields an approximate $2X_0$ total thickness for all particle trajectories. The end and side views of the detector are shown in Fig. 1. The space budget for each layer is shown in Table I.

Items	Detector Space (Radii) (mm)	Clearance (Radii) (mm)	Length (mm)	Stereo Angle (degree)
Solenoid	– 707.8	–	2730.0	–
Lead	707.8 – 714.3	–	vary	–
Air gap	714.3 – 718.0	–	–	–
Axial layer	718.0 – 725.5	725.5 – 729.0	2730.0	0.0
U stereo layer	729.0 – 736.5	729.0 – 740.0	2730.0	22.98°
V stereo layer	740.0 – 747.5	747.5 – 759.0	2730.0	23.29°
Calorimeter	759.0 –	–	–	–

TABLE I. Basic geometry of the central preshower detector.

B. The Pre–radiator

The pre–radiator of the preshower detector is composed of the solenoid and the tapered lead. The radiation length of the solenoid as a function of pseudorapidity for particles originating

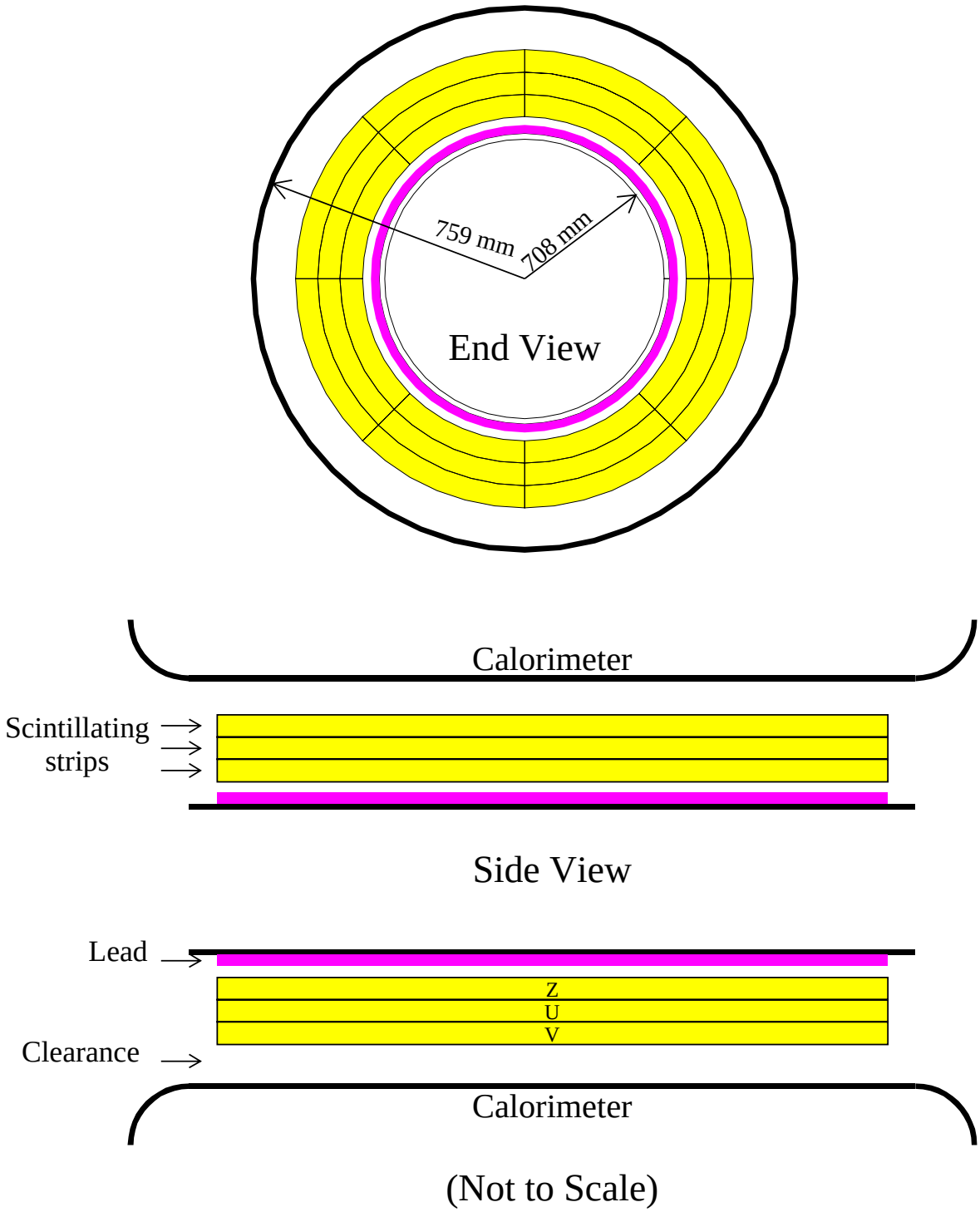

FIG. 1. Schematic end and side views of the central preshower detector for the DØ upgrade.

from the center of the detector. is shown in Fig. 2(a). To make a constant 2 radiation lengths for all particle trajectories, a tapered lead will be installed on the solenoid. Figure 2(b) shows the thickness of the lead as a function of the z position along the beam line. In reality, the lead will be stepped with the step size approximately equal to the beam size along the z direction. The radiation material in the solenoid is mostly due to the aluminum which is distributed over 17 cm of radial space. This configuration of the material in the solenoid makes the solenoid a non–ideal pre–radiator. First, the low ratio of the radiation length and nuclear interaction length of the aluminum means that the solenoid also consists of about 20% of the nuclear interaction length as shown in Fig. 2(a) (dotted line). Therefore, a significant fraction of charged pions start hadronic showers in the solenoid. Secondly, the thick solenoid allows electromagnetic showers in the solenoid to spread. As discussed in sec. III, both effects will reduce the power of the detector to separate electrons from background.

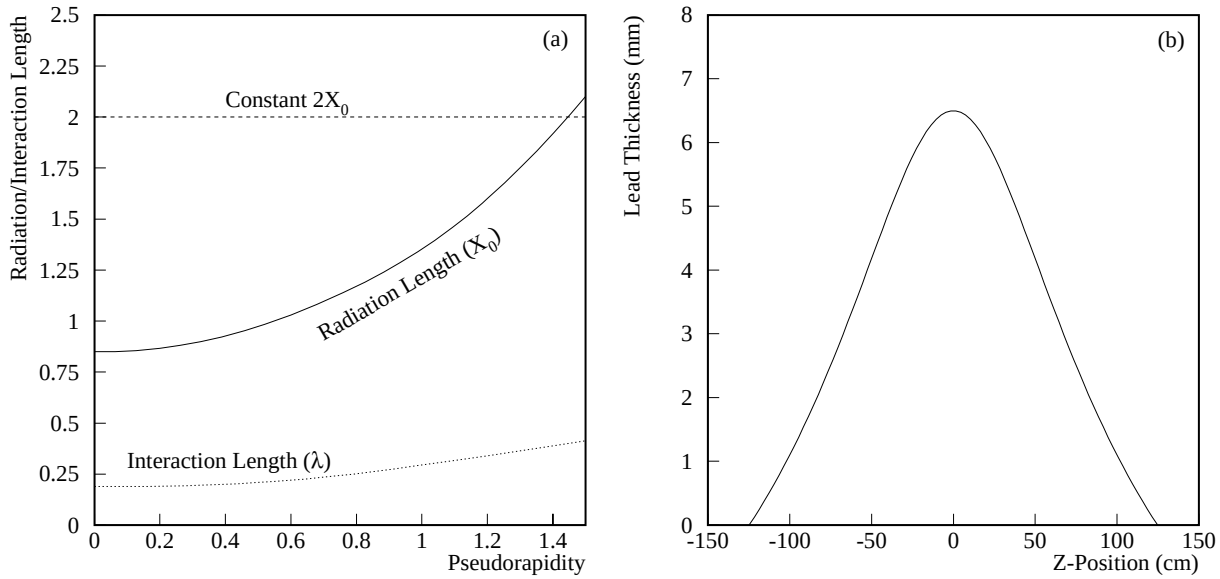

FIG. 2. (a) The solenoid's radiation and nuclear interaction lengths as functions of pseudorapidity and (b) the thickness of the lead needed to yield a constant $2X_0$ for all particle trajectories.

C. The Detector

To facilitate the detector construction, each layer will be made into 8 octants each 273 cm long. The WLS fibers will be splitted at $z = 0$ and are connected to the clear fibers at both end of each octant. The fiber splitting at $z = 0$ effectively haves the occupancy for each channel and therefore make the detector less vulnerable to high rates. The clear fibers from either end of octants will be grouped together to form one bundle. There will be 24 octants and 48 clear–fiber bundles for the central preshower detector.

The information from the axial strips of the preshower detector will be combined with the

fiber tracker information at Level–1. Since fibers are not splitted for the fiber tracker, the signals from the two WLS fibers of the same axial strip of the preshower detector will have to be combined electronically before matching with the tracker can be made. Since 80 trigger sectors in ϕ is planned for the fiber tracker, the preshower detector will also be subdivided into 80 sectors, with 10 sectors in each octant. In addition, there will be 16 strips in one sector (2×160 readout channels per octant) resulting a total of 7680 readout channels for the detector. The fiber–fiber connectors are designed to match the segmentation of the detector, with 16 channnels per connector. The 16–channel segmentation for the connector at the detector side also matches that proposed at the VLPC end.

We have investigated two basic cell geometries. The first one shown in Fig. 3(a) involves machining square strips out of a large scintillating sheet with neighboring strips separated by isolation grooves. In this design, two staggered layers are needed for each axial and stereo view to reduce detector inefficiency. The second design is to replace square strips with triangular strips, which can either be machined from large scintillating sheets (shown in Fig. 3(b)) or be made through extrusion (shown in Fig. 3(c)). This design eliminates the need for two staggered layers of square cross section, making the detector more compact. In addition, it will improve the position resolution for minimum ionizing particles as a result of the light sharing between two neighboring strips. Both machined square and triangular strips have been tested using cosmic–ray muons. The test results are summarized in sec. IV. The test results indicate that both geometries have a considerable margin in achieving the performance specifications of the preshower detector. However, given their other advantages and comparable electron identification performance discussed in sec. III, the triangular strips have been chosen for the baseline design.

The machined and extruded triangular strips are in many ways very similar. While the extrusion allows one to place the key–hole grooves in the center of the strip without introducing significant additional inactive space, the machining has the advantage of an automatic strip–to–strip registration provided by the precision milling machine. However, the decision has been made to pursue the design with the extruded strips. The detailed geometric dimension of the strip is described in sec. V.

The *uv* stereo angles are adjusted to ease the detector installation on the solenoid. Octants of all three–layers will be precisely aligned at both ends so that any octant in a given layer will cross three octants from any other layer. Given the radii of each layer and the length of the octant, this design leads to stereo angles of 22.99° for the inner stereo layer and of 23.29° for the outer stereo layer as shown in Table I. Detailed design is described in sec. V.

D. Readout & Trigger

Scintillation light produced by showers will be collected by the WLS fibers and piped through clear fibers to the photodetectors outside the magnet. A typical length for the clear fibers will be 8–11 meters. The WLS and clear fiber will be joined by connectors at the end of each fiber. Visible light photon counters (VLPC) [4], currently under development at the Rockwell International Science Center, will be used as photodetectors. This solid state device is capable

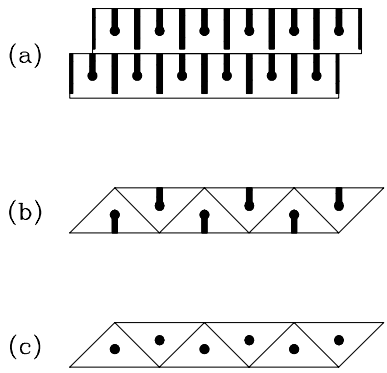

FIG. 3. End views of (a) machined square strips, (b) machined triangular strips and (c) extrusion triangular strips. The WLS fibers will be housed by the key–holes in the strips. The neighboring strips are connected by the small amount of scintillator for machined square and triangular strips.

of high–rate, single photon counting with a quantum efficiency greater than 70%. Typically, the VLPC has a gain of about 10^4. As discussed in sec. VII, the high rate capability of the VLPC could be a problem and needs to be investigated. Before the VLPC signals are sent to SVX–II chips for amplification and digitization, they will be split into two channels each by special chips designed for the preshower to allow for fast trigger pick-off and to effectively extend the dynamic range of the readout system. To facilitate the Level–1 electron trigger discussed in sec. III, the readout for the axial layer will be integrated with the fiber tracker readout.

III. SIMULATION RESULTS

The simulation effort has been concentrated on understanding the detector response to electromagnetic and minimum ionizing particles, as well as electron identification both on–line and off–line. The square cell geometry was initially considered and subsequently dropped in favor of the triangular strips based on the results from the cosmic–ray tests and simulation. The cosmic–ray results for both square and triangular strips are discussed in sec. IV. The two geometries are comparable in terms of light yield, uniformity etc. Simulation shows that the key functions of the preshower detector, such as the Level–1 electron trigger and off–line electron identification, are not compromised by replacing the square strips with triangular strips. Due to the limited resources, not all simulation has been repeated for triangular strips. Consequently, some of the simulation results presented below are for the square geometry. Furthermore, the exact magnetic field map inside the solenoid and the preshower detector was not implemented in the simulation. Instead a constant 2 Tesla magnetic field was assumed to present throughout the solenoid and the preshower detector. The strong field has the effect of spreading out electromagnetic showers as discussed below. In reality, the field inside the preshower detector is estimated to be a few hundred kGauss. Finally, two different stereo angles were used in the simulation: 20° for the square strips and 90° for the triangular strips. In all cases, the fiber–to–fiber space in each layer used in the simulation is about 4.7 mm. This segmentation results in 960 channels for the axial view of the triangular geometry and 2×960 channels for

the square geometry. Unless otherwise specified, the fibers were not splitted at $z = 0$ in the simulation.

A. Detector Responses

We have studied detector responses to minimum ionization and electromagnetic particles. For these studies, single–particle Monte Carlo events are generated and simulated. Investigation of the single particle response of the detector is the first step towards an understanding of the detector. We summarize the studies below.

1. Minimum Ionization Particles

Minimum ionization particles such as muons and charged pions generally only deposit dE/dx energy loss in the preshower detector. The total energy deposited by $E_T = 10$ GeV muons and charged pions at $\eta = 0$ in the axial layer of the preshower detector is shown in Fig. 4 for triangular geometry. One energy unit corresponds to the most probable energy loss by muons, i.e., 1 MIP=0.66 MeV. The energy deposited by particles at $\eta = 1$ is approximately a factor of two of that at $\eta = 0$ due to the difference in the amount scintillator traversed (angle effect). Compared with the energy deposited by muons, the distribution by charged pions has a long high-energy tail. This is due to the fact that the solenoid consists of about 20% nuclear interaction length and thus many charged pions interact in the solenoid. About 27% of the charged pions as compared with 2% of muons deposit more than a 5 MIP energy loss in the preshower detector.

2. Electromagnetic Particles

Most electrons and photons will develop electromagnetic showers in the pre–radiator, and therefore deposit a large amount of energy in the preshower detector. Figure 5(a) shows the distribution of the total energy and the maximum cell energy deposited in the preshower detector by $E_T = 10$ GeV electrons in units of the most probable energy loss by muons for the triangular geometry. On average, about 35% of the total energy deposited in the detector is registered in the highest energy cell. The normalized energy deposition as a function of cell number for $E_T = 10$ GeV electrons is shown in Fig. 5(b), where the cell 0 is the cell with the highest energy deposition. The order of the cells is mirrored such that the cell -1 is the cell with the second highest energy deposition. The error bar represents the spread in the energy distribution of the respective cell. The large error bar indicate that the electromagnetic shower has a wide fluctuation at this early stage of the shower development. Nevertheless, the shower cores are generally narrow. The total energy in the three cells centered at the maximum cell accounts for 50% of total energy deposition. To see the effect on the shower broadening due to the magnetic field, the shower profile when the field is set to zero in the simulation is shown as dotted line.

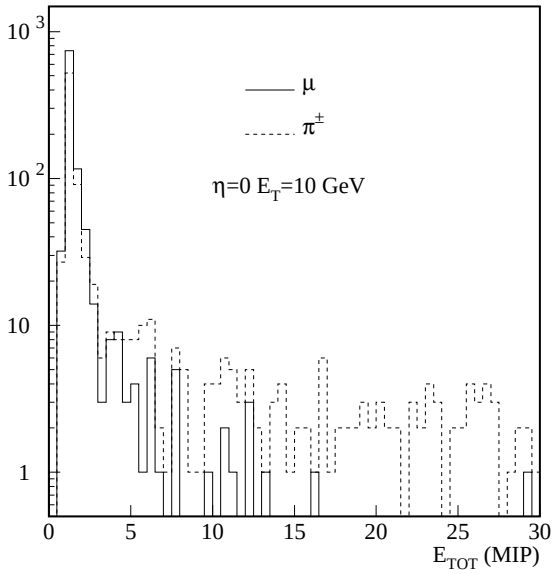

FIG. 4. The total energy deposited in the axial layer of preshower detector by $E_T = 10$ GeV muons and charged pions in units (MIP) of the most probable energy loss by muons (1 MIP=0.66 MeV). The long tail in the distribution for the charged pions is due to the hadronic interaction in the pre–radiator.

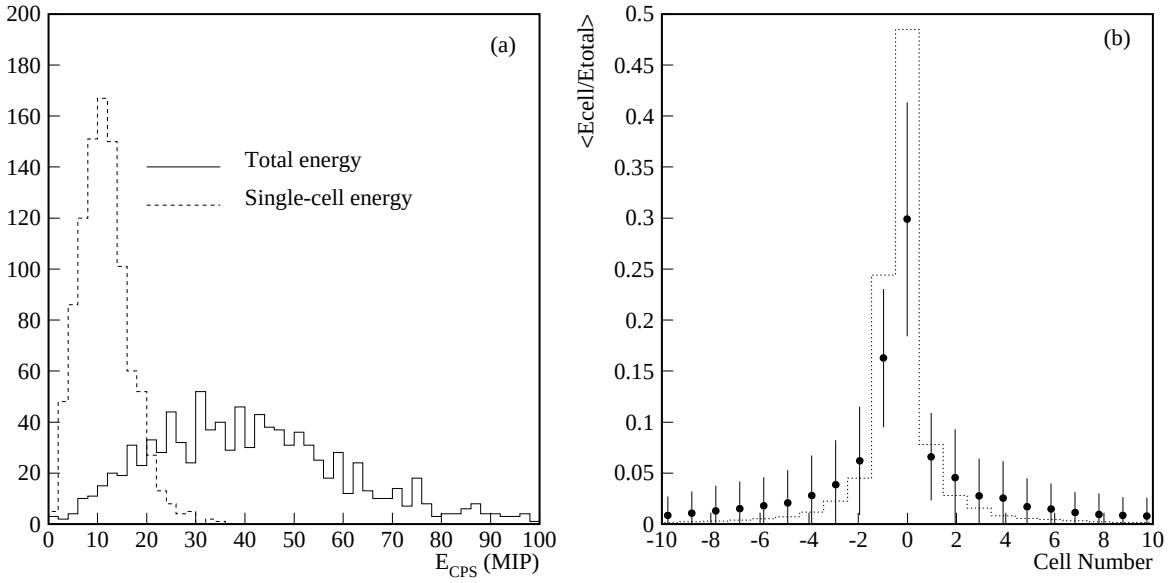

FIG. 5. (a) The distributions of the total and the maximum single–cell energy deposited in the axial layer of the preshower detector by $E_T = 10$ GeV electrons at $\eta = 0$ for the triangular geometry. (b) The normalized energy deposition as a function of cell number centered around the maximum cell. The error bar represents the spread in the normalized distribution. The dotted line is the expected distribution when $B = 0$.

B. Detector Resolutions

Position and energy measurements of the electromagnetic showers are critical for electron identification. Most background for electrons is either due to a single charged pion or due to overlap of charged and neutral pions. Good position and energy resolution allows us to do precise matches between the track–shower position and between electromagnetic energy (E) and momentum (p) to reduce these background.

1. Position Resolution

While the DØ calorimeter will provide superior position resolution for high E_T electrons, the finely segmented preshower detector will contribute significantly to the position measurement of low E_T electrons, such as those from b–quark decays. Figure 6 shows the expected $r\phi$ and rz position resolution of the preshower detector for $E_T = 10$ GeV electrons. The results are for the triangular geometry with a 90° stereo angle. For a 20° stereo angle, the rz resolution is expected to be a factor of two worse. The position of the electromagnetic shower was calculated using the positions of the three cells centered around the cell with the maximum energy deposition:

$$(r\phi)_{\rm shower} = \frac{\sum_i E_i (r\phi)_i}{\sum_i E_i}; \qquad (rz)_{\rm shower} = \frac{\sum_i E_i (rz)_i}{\sum_i E_i}$$

Studies show an improvement of as much as 20% in the resolution can be achieved by optimizing the power of the energy weights. The long tail in the $r\phi$ distribution is due to the presence of 2 Tesla magnetic field. For comparison, the dotted histogram ($\sigma = 0.9$ mm) in Fig. 6(a) represents the expected position resolution when the magnetic field was turned off completely. The position resolution will improve as electron energy increases.

2. Energy Resolution

The addition of $1X_0$ of material in the solenoid coil (normal incidence) in front of the cryostat walls would be expected to degrade the electromagnetic energy resolution, especially for low E_T electrons at high pseudorapidity [1]. However, simulation shows that there is minimal degradation of energy resolution if the information from the preshower detector is included. The expected energy resolutions of the upgraded DØ calorimetry for $E_T = 2$ GeV for the cases with and without a preshower detector is shown in Fig. 7(a). As expected, the addition of a preshower detector improves the energy resolution. It should be noted that the preshower correction is expected to decrease as electron energy increases. Figure 7(b) shows the expected

[1]The solenoid, together with the cryostat of the DØ central calorimeter will consist of more than two radiation length material for particles at normal incidence and more than four radiation lengths for particles at $\eta = \pm 1$ before the calorimeter.

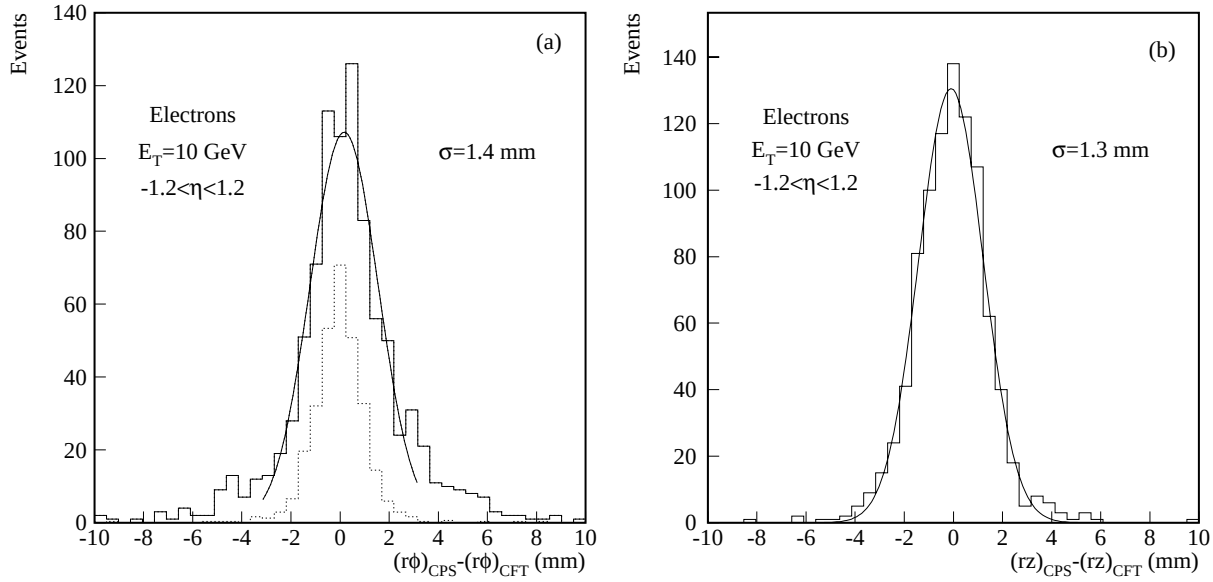

FIG. 6. Simulated position resolution of the preshower detector for $E_T = 10$ GeV electrons: (a) the resolution in $r\phi$ and (b) the resolution in rz. A 90° stereo angle was used in the simulation. The rz resolution for a 20° stereo angle is expected to be a factor of two worse than that shown in (b). The dotted histogram in (a) represents the distribution ($\sigma = 0.9$ mm) when the magnetic field was turned off in the simulation.

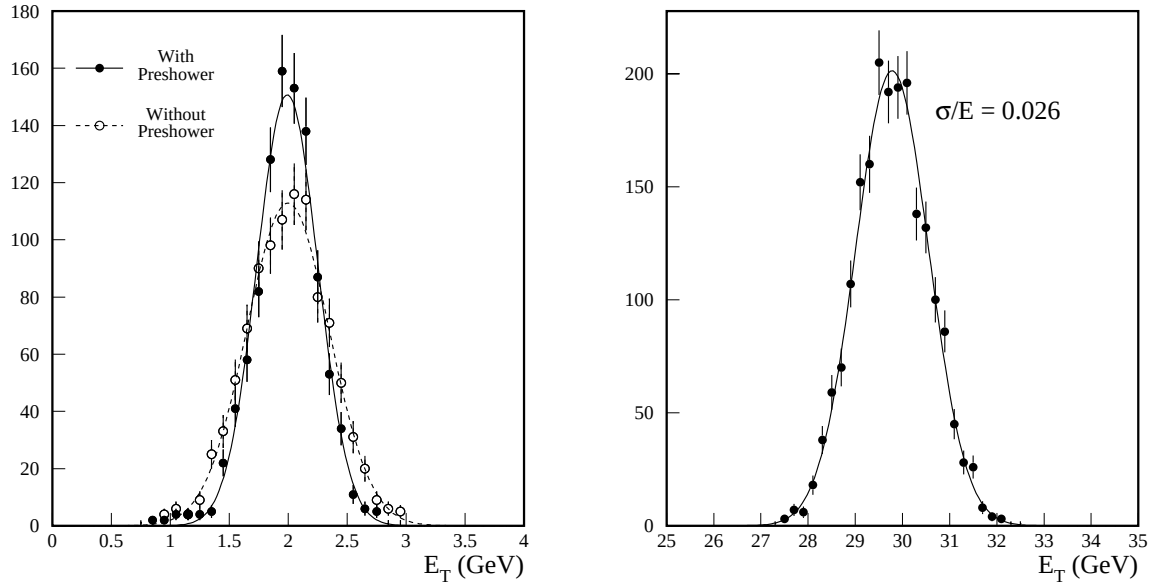

FIG. 7. The Monte Carlo simulation of the upgraded DØ calorimetry: (a) response to $E_T = 2$ GeV electrons at $\eta = 1$ for the cases with and without a preshower detector for the DØ upgrade. Without a preshower detector, the resolution is expected to be 18% while it is 13% with a preshower detector, and (b) response to $E_T = 30$ GeV electrons at $\eta = 1$ with a preshower detector.

energy resolution of the upgraded DØ calorimeter with a preshower detector for $E_T = 30$ GeV electrons.

C. Electron Identifications

Good electron identification is essential for studying high mass and high p_T phenomena, as well as B-physics. Like electron identification with the current DØ detector, the primary electron selection for the upgraded DØ will be based on the fine-grained DØ calorimeter. However, the preshower position and energy information and the capability for matching between electromagnetic energy in the calorimeter with the momentum measured by the magnetic tracker will provide an additional means of rejecting background. These two tools are often complementary. The E/p matching will work well in the region where both E and p are well measured and it is a powerful indicator of $\pi^{\pm} - \pi^{0}$ overlap. It will fail in cases where genuine electrons are close to jets, as for semi–electronic b–quark decays. The fine spatial resolution of the preshower detector will allow for precise matching with the tracking system to reduce the background from $\pi^{\pm} - \pi^{0}$ overlaps for electrons close to jets.

1. On–line

The preshower detector with its fast readout will enable us to separate electrons from charged pions at the Level–1 trigger. In this section, we discuss a high p_T electron trigger using the information from the preshower detector.

Most electrons will develop electromagnetic showers in the pre–radiator and therefore deposit a large amount of energy in the preshower detector. On the other hand, most charged hadrons (mostly $\pi^{\pm}$'s) will register energy deposition corresponding to minimum ionizing particles. Therefore, the difference in energy deposition in the preshower detector will enable us to separate electrons from charged pions.

The energy deposition in a single axial triangular strip in units of energy deposition by minimum ionization particles by $E_T = 10$ GeV electrons and charged pions are compared in Fig. 8(a). While the energy deposition by the charged pions peaks strongly at 1 MIP, the energy deposition by electrons has a broader distribution and generally is greater than that of charged pions. A requirement on a minimum energy deposition in the preshower detector reduces the $\pi^{\pm}$ background significantly, while maintaining good efficiency for electrons. Figure 8(b) shows electron efficiency and pion rejection as functions of the energy requirement. A 4MIP energy requirement rejects 90% of the charged pions while retaining 95% of electrons. Due to the angle effect, it should be noted that the rejection is reduced to about 80% for charged pions at $\eta = 1$. A large fraction of the charged pions satisfying the requirement were due to the start of a hadronic shower in the solenoid. Consequently, this background is irreducible with a simple threshold cut. This is true even if one sums the cell energy around the maximum cell and imposes an energy requirement on the cluster.

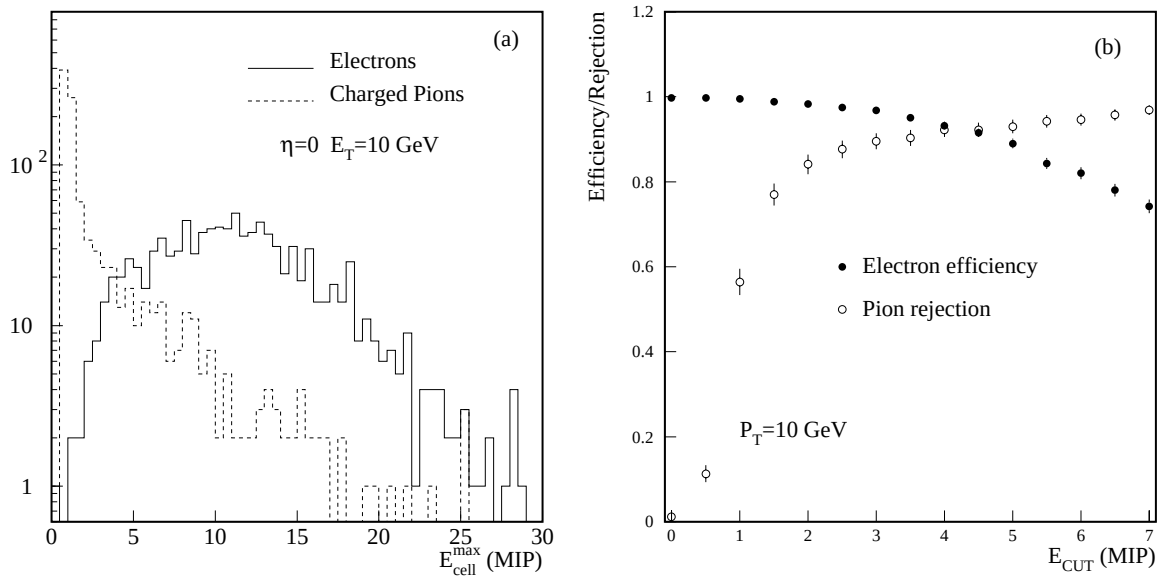

FIG. 8. (a) The distribution of the highest single–strip energy deposited in the preshower detector by electrons and charged pions for the triangular geometry. (b) Electron efficiency and pion rejection as functions of single strip energy cut.

Shower profile information in the preshower detector is another possible tool for separating electrons and charged pions. However as shown in Figure 5(b), the large fluctuation in the shower profile precludes any algorithm at Level–1 trigger utilizing the shape information for separating electrons and charged pions with high efficiency for electrons and high rejection for charged pions.

Neutral hadrons that decay into photons (mostly π^0's) will register signatures identical in the preshower detector to that of electrons. However, spatial matching between the clusters in the preshower and the tracks in the tracker will allow us to separate electrons from neutral pions. The integration between the preshower and scintillating fiber tracker readout enable us to match the preshower information with the tracker information at Level–1. This is especially important for DØ since the huge cost of upgrading the calorimeter trigger electronics unfortunately precludes us from matching calorimeter and tracker information at Level–1.

2. Off–line

While the electron identification on–line focuses on electrons with relatively high p_T, off–line electron identification deals with both low p_T (those from b–quark decays) and high p_T (those from W/Z decays) electrons. In fact, the aid in electron identification provided by the preshower detector is most significant for low p_T electrons. The off–line electron identification algorithm starts with clustering preshower hits, followed by a spatial match between preshower cluster and fiber tracker and finally the match between track momentum and calorimeter energy.

As shown in Fig. 5(b), the electromagnetic showers are generally very narrow. Most of the shower energy is deposited in three strips. The preshower cluster algorithm begins with seed cells containing more than a 4 MIP energy deposition. The energies of the neighboring cells are summed to form cluster energy. The position of the cluster is calculated using cell positions weighted by their energies. The algorithm is applied to axial and stereo strips independently.

The clusters reconstructed from axial strips are matched with the Monte Carlo tracks in $r\phi$. The difference in $r\phi$ between the cluster position and the extrapolated track impact position is is calculated for all combinations. A cut in the difference is applied. Only those clusters with matched tracks passing this cut are retained. The tracks are then matched with stereo clusters in rz. Again, the differences in rz between the tracks and the stereo clusters are calculated and are subject to a cut. Finally, E/p matches are applied for tracks associated with axial and stereo clusters.

We have studied low p_T electron identification for the old square geometry. For this study, ISAJET [5] $b\bar{b}$ and QCD dijet events with $p_T > 20$ GeV/c were simulated using UPG_GEANT. For the $b\bar{b}$ events, one of the b–quarks is required to decay into an electron with $p_T > 5$ GeV/c in the geometrical acceptance of the central preshower detector. The analysis began with the $b\bar{b}$ and QCD dijet samples of the same statistics. The requirements on preshower cluster energy and cluster-track space matches reject 90% of QCD dijet events while retaining 80% of $b\bar{b}$ events. Most of the remaining background is due to early showering charged pions. Combined with the E/p matching between the track and calorimeter cluster, a rejection of 100:1 is achieved with 73% efficiency for $b\bar{b}$ events without using shower shape information. Figure 9(a) shows the difference between preshower cluster and track positions in $r\phi$ and Fig. 9(b) compares [2] the E/p for electrons and background. The efficiency and rejection for each requirement are shown in Table II. This level of efficiency and rejection should be adequate for tagging b–quark jets from $t\bar{t}$ decays. With shower shape information from both the calorimeter and the preshower, another factor of ten rejection should be achievable. Another possible handle is the isolation cut. While the isolation cut is difficult to apply to the calorimeter for low p_T electrons due to hadronic showers, it should be less of a problem in the preshower detector.

D. Other Considerations

1. Trigger Rejection

The preshower information will not only help to reject background due to charged pions, it will also reduce the rate of the Level–1 fiber tracker trigger due to fake tracks. In general,

---

[2]The calorimeter was not simulated for the study. The energy E used in the study is the sum of all electromagnetic energy and 30% of hadronic energy within a cone with a 7° half opening angle. The electromagnetic and hadronic components are smeared using the resolution functions $\frac{\sigma}{E} = \frac{15\%}{\sqrt{E}} \oplus 3\%$ and $\frac{\sigma}{E} = \frac{50\%}{\sqrt{E}} \oplus 5\%$ respectively.

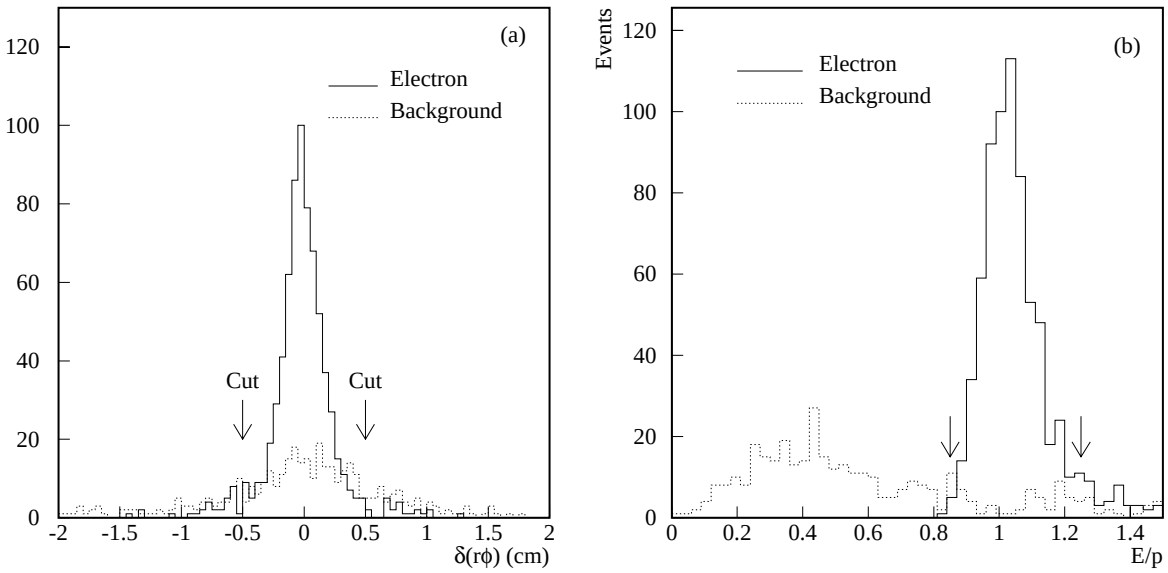

FIG. 9. The distributions of (a) the difference between the $r\phi$ shower position measured by the preshower detector and that extrapolated from the track and (b) the energy–momentum ratio for electrons and their background. Electron and the background distributions are obtained from $b\bar{b}$ and QCD dijet samples respectively. The simulation was done for the square geometry.

a match requirement between the Level–1 fiber trigger track and the preshower hit will reduce the Level–1 electron trigger rate significantly. Studies of ISAJET [5] two–jet events show that the information from the preshower provides a factor of 3–5 reduction in the Level–1 electron trigger rate as demonstrated in Fig. 10. In this study, the trigger track is required to match to the preshower hit within ± 1 preshower strip. About 70% of QCD events passes a 1 MIP cut and 20% passes a 4 MIP cut. To examine the source of the trigger, the same events were simulated with π^0's removed. In this case, the fractions of events passing the preshower requirement is about 13% for a 4 MIP cut. The small difference at the high MIP cut for the cases with/without π^0 in the simulation implies that the background is dominated by early interacting charged pions rather than by the overlaps of charged and neutral pions. Therefore, an additional preshower Level–1 trigger in rz may not reduce the background significantly. Although the simulation was done for the old square geometry, we expect a similar result for the triangular geometry.

2. γ/π^0 Separation?

The fine segmentation of the preshower detector should also help photon and neutral pion separation. Simple calculation shows that the two photons from π^0 decay will have their shower centroid registered in two different cells for π^0 energy up to 10 GeV. Therefore, the preshower information should contribute significantly for γ/π^0 separation in Run II. Obviously, it needs to be better understood through Monte Carlo simulation.

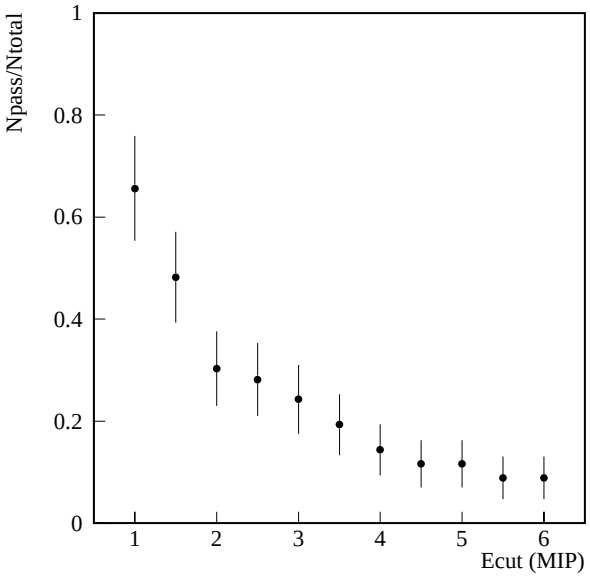

FIG. 10. Fraction of ISAJET events which pass the Level–1 fiber tracker trigger passes the preshower energy requirement as a function of the preshower threshold. Note that the simulation was done for the old square geometry and for the old tracker kappa trigger bin.

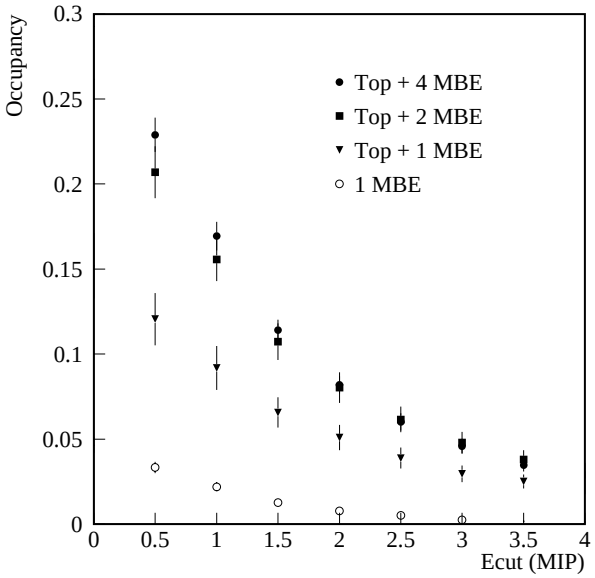

FIG. 11. The expected occupancy as a function of the energy deposition in the preshower strip for minimum bias events and $t\bar{t}$ events with different number of minimum bias events overlaps. The simulation was done assuming the strips are broken into two parts at $z = 0$. The occupancy for the baseline design with 250 cm long strips is expected to be factor of two higher than what is shown in the figure.

Requirement	$b\bar{b}$	QCD
No cut	100%	100%
$E_{\rm cluster}^{\rm axial} > 10$MIP	94%	21%
$r\phi$ match, $\delta(r\phi) < 5$ mm	87%	12%
rz match, $\delta(rz) < 15$ mm	80%	7%
$0.85 < E/p < 1.25$	73%	0.8%

TABLE II. Fraction of the $b\bar{b}$ and QCD dijet events passing each cut. A combination of requirements on preshower energy, preshower–tracker space match and the E/p match results a QCD fake rate of 0.4%/jet with high efficiency for jets with real electrons.

3. A Low p_T Di-electron Trigger?

Our effort in understanding the Level–1 electron trigger has been primarily directed towards the single high p_T (> 10 GeV) electron trigger. In principle, we can lower the p_T threshold if two electrons are required in the trigger. Such a trigger will be very useful for $J/\psi \to e^+e^-$ events. The effectiveness of such a trigger without saturating the trigger bandwidth remains to be investigated.

4. Occupancy

At a luminosity of $\mathcal{L} = 2 \times 10^{32}$ cm^{-2}s^{-1} with 132 ns bunch spacing, on average there will be 1.3 interactions per crossing. To achieve the design performance of the detector, the occupancy of the preshower detector has to be kept low, where the occupancy is defined as the ratio between the number of strips with hits and the total number of strips. Figure 11 shows the expected occupancies for $t\bar{t}$ events with different number of minium bias events (MBE) overlaps as functions of the energy deposition for the axial strips. The axial strips are assumed to be broken into two parts at $z = 0$. A top mass of $M_T = 200$ GeV was used in the simulation. While the minimum bias events contribute little to the occupancy for energy above 4 MIP and therefore have a weak effect on the preshower Level–1 trigger, it has a dramatic effect on the occupancy at lower strip energy. This will no doubt affect the off–line analysis using shower shape or isolation information. For the baseline design with 250 cm long axial strips, the occupancy from minimum bias events is 5% at a threshold cut corresponding to one MIP. As discussed in sec. VII, this level of occupancy coupled with the high minimum bias event rate has a dramatic impact on the operation of the VLPC of the preshower readout.

IV. SCINTILLATORS AND FIBERS

A. Scintillator Properties

Two types of scintillator technologies have been considered for usage in the DØ preshower detector: megatile and extruded. While the technologies involved in manufacturing the two types of scintillators are quite different (discussed below), their spectral performance and radiation resistance are quite similar.

Before the demise of the SSC, considerable effort had been expended in investigating scintillator and WLS combinations which resulted in high light yields and a high degree of light-output stability in relatively high radiation environments. One combination which has proven to be popular is Bicron [6] BC-404 scintillator in conjunction with Kuraray [7] Y-7 and Y-11 WLS or Bicron BCF-91A WLS fiber. BC-404 is a polyvinyltolulene (PVT) based scintillator with p-terphenyl (pT) and di-phenly(stilbene) (DPS) as primary and secondary dopants respectively. The concentration of these dopants is not known. All of the above mentioned wavelength shifters are made of the proprietary dopant K27 at different (and often unknown) concentrations. The fluorescence spectrum of DPS is given in Fig. 12, as is the fluorescence spectra of K27. The emission peak of K27 (including the effects of self-absorption) is ~ 500 nm [8].

PVT has a refractive index of 1.58, a density of 1.032 g/cm^3 and a coefficient of linear expansion of 7.8×10^{-5}/°C below 67°C. Bicron is able to form sheets 5 mm thick (with a maximum transverse extent of 63×203 cm) with tolerances of +0.56/-0.46 mm. Larger sheets have poorer tolerances. It is likely that preshower tiles will be on the order of 120×120 centimeters and thus this thickness variation is of some concern. The extruded strips will be made of polystyrene (PS) plastic. This material has an index of refraction of 1.60 and a density of 1.05 g/cm^3. These basic properties of the two plastics are given in [9]. The intrinsic light yield of polystyrene is $\sim 10 - 15\%$ less than PVT [10]. In addition, the visible light yield is dependent on the primary and secondary fluor concentrations. The concentrations in BC-404 is unknown, but the concentration in the extruded scintillator has been chosen as a 'best-guess' approximation of BC-404. Thus it is not possible to *a priori* determine which would have the best light yield, although it is possible to state that the spectral output of the two choices is essentially the same.

While one can purchase BC-404 scintillator from an established vendor, we must manufacture the extruded scintillator. Researchers at Fermilab [19] have pioneered this technology. Details on their manufacturing procedure are not generally available in the literature, but the general techniques are clear.

Pellets of polystyrene plastic are impregnated with primary and secondary fluors. These pellets are of the general size of cylinders 3 mm in diameter and 5 mm high. In order to make strips, these pellets are given to the RDN Corporation [20] to be extruded. This technology is very mature. We have extruded strips 2 meters long and they have $\sim$ 50-75 μm tolerances in the important dimensions. Longer and shorter strips are trivial variations on the current successful efforts. If the extruded design option is chosen, we will need to manufacture a new extrusion die, but this should pose no problem. We consider the manufacturing R&D of these

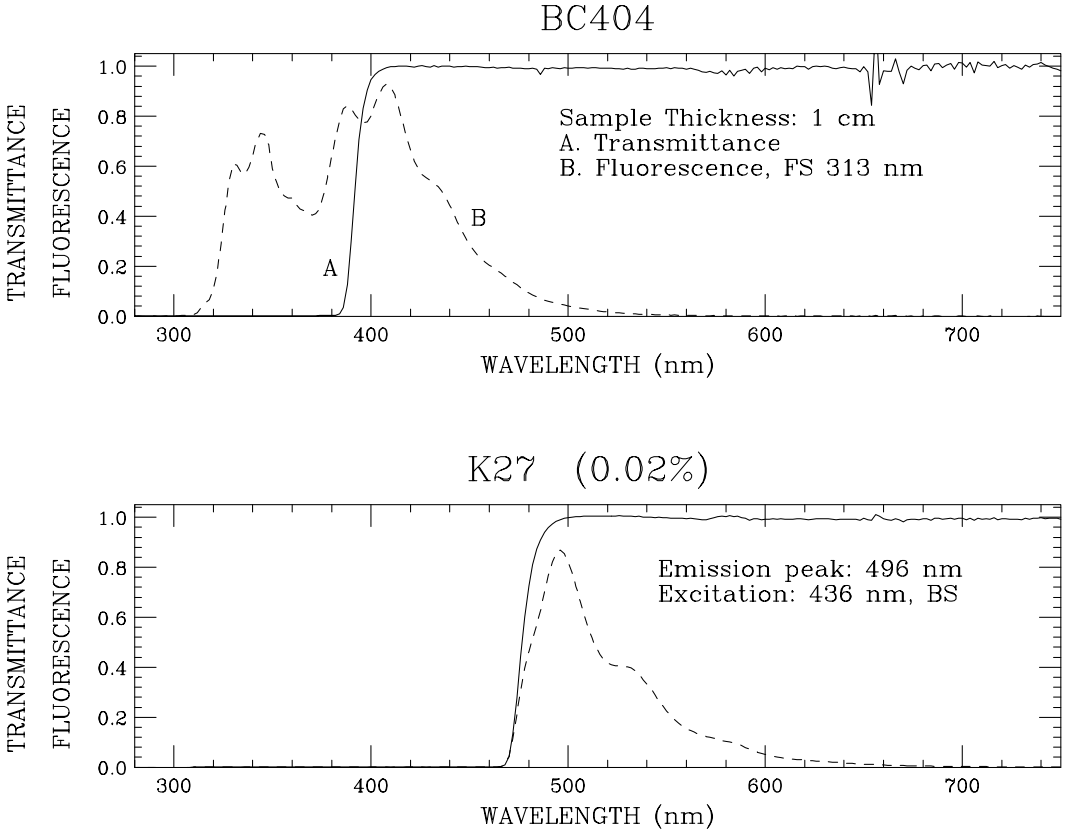

FIG. 12. The top plot is the fluorescence spectrum of BC-404, achieved by illuminating the scintillator with a 313 nm light source on the front edge. The two peaks near 350 nm are from pT, the two peaks near 400 nm are from DPS. The light transmission curve is also shown. The light one sees from BC-404 is a convolution of the emission and transmission curves. The bottom plot is a similar result for K27. However, in this case, the sample was irradiated from the back side. Thus the light spectrum shown already convolves the fluorescence of K27 with its transmission. In fact, K27 emits shorter wavelength light, but self absorbs it. Figure courtesy of Anna Pla-Dalmau

strips to be complete. Light yield and alignment tests still need to be completed.

B. Radiation Damage

Radiation damage is defined to be a loss of light output as a function of radiation dose. The relationship between light loss and radiation dose is exceedingly complex. Dose rates, total dose, plastic type, fluor type and concentration, environment (temperature and atmosphere), and recovery time are just some of the possible contributing factors. Thus one must use published results with caution.

Radiation damage does not affect all wavelengths of light equally. Longer wavelengths ($\sim$ green or red) are much less affected than shorter wavelengths ($\sim$ blue or violet). This point is shown in Fig. 13. In this plot, a polystyrene plastic disk containing K27 at a concentration of 0.02% by weight has been irradiated with 10 Mrads. Four curves are present: (A) is the light transmission before irradiation, (B) is the light transmission immediately after irradiation, (C) is the light transmission after 10 days of annealing in air, and (D) is the light transmission after an additional 14 days of annealing in a pure oxygen environment. Several things must be noted. The first is that shorter wavelength light is affected more than longer wavelength. The second thing is that the light transmission seems to recover over time. In the above test (detailed in [11]), the dose rate was quite high (1.8 Mrad/h), thus the damage was massive and quick. When removed from this high radiation environment, the light output is able to recover until only a small residual amount of damage remains. In the event of a low dose rate irradiation, the light yield recovers as the damage is caused and thus the actual damage is much less than that seen in the high dose rate tests. A secondary complication concerns the fact that the radiation damage seems to involve the oxygen gas suspended within the plastic. Therefore in a high rate dose, this suspended oxygen is quickly depleted and the diffusion rate into the plastic is small enough that the 'fuel' for the radiation damage is soon gone. Thus in a low rate dose, the diffusion of oxygen into the plastic is often faster than the local depletion and the radiation damage is allowed to proceed. So while the maximum high rate damage far exceeds that seen in the low dose rate case, the residual damage is usually greater in the low dose rate case. Because of the time involved in doing low dose rate studies and because the difference in the residual damage in both cases is relatively small, high rate studies are typical. Reference [12] contains more discussion of these effects.

With these substantial caveats in mind, we may then address the question of the radiation tolerances of the materials to be used in the DØ preshower detector. A literature search provides no study which tests precisely the correct materials in the right form and under the proper conditions, and manpower and time considerations preclude that we undertake such a study. We are therefore required to use the most relevant previous studies and infer the required quantities.

Radiation damage can take two forms: (1) The intrinsic light yield can be reduced and (2) The attenuation length can be reduced. Often both factors are present. In the current design, blue light must travel on the order of a centimeter and green light must travel on the order of 1.5 meters. Thus it is likely that the intrinsic light loss is more relevant for the scintillator

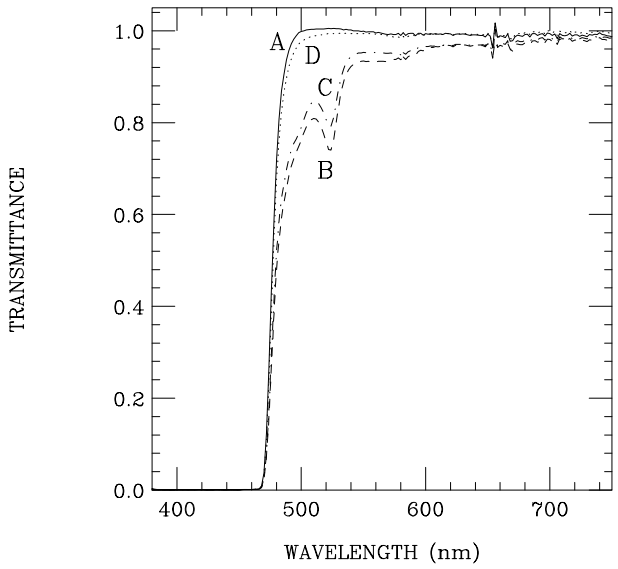

FIG. 13. The light transmission of a 0.02% solution of K27 dissolved in polystyrene as a function of wavelength for different times between the irradiation and the measurement. The radiation dose was 10 Mrad at a rate of 1.8 Mrad per hour. (A) is the light transmission before irradiation, (B) is the light transmission immediately after irradiation, (C) is the light transmission after the sample annealed in air for 10 days, (D) is the light transmission after an additional 14 days of annealing in pure oxygen. Figure courtesy of Anna Pla-Dalmau.

and the attenuation length is more relevant for the green fiber. In reference [13], the effect of radiation damage is modelled in a particularly tractable way. Before irradiation, light output is given as $I_{\mathrm{non-irradiated}}(z) = I_o e^{-z/\lambda}$, where $I_{\mathrm{non-irradiated}}(z)$ is the light output as a function of distance from the light source, I_o is the light seen at $z = 0$, λ is the attenuation length of the material (including intrinsic absorption and geometrical effects), and z is the distance from the light source to where the light is read out.

Using the ansatz where both intrinsic light yield and attenuation length can change, one can write the light exiting the detector after radiation as:

$$I_{\mathrm{irradiated}} = (1 - \beta D) e^{-z/\mathcal{Z}} I_{\mathrm{non-irradiated}} \tag{1}$$

where β describes the loss in light production per radiation dose, D is the radiation dose and $\mathcal{Z}$ is a radiation-induced attenuation length which can be modelled as

$$1/\mathcal{Z} = a \cdot D e^{-t/\tau} + b \cdot D \tag{2}$$

where the first term describes the temporary damage of the scintillator which heals with characteristic time τ, and the second term is the permanent damage (after all possible healing is done). One may then measure the interesting quantity b by irradiating the sample with a known dose, letting the sample anneal and recover to the maximum extent possible and then measure the observed (post-irradiation) attenuation length, $\lambda_{\mathrm{irradiated}}$. One can then extract the effect of the radiation by

Material	b (%/Mrad)	$(1/\mathcal{Z})$ cm^{-1}rad^{-1}
SCSN-38	4% ($\pm$1%)	1.1×10^{-8} ($\pm$8%)
K27	0% ($\pm$1%)	$< 0.2 \times 10^{-8}$ ($\pm$5%)

TABLE III. Radiation damage parameters for SCSN-38 (a Kuraray polystyrene scintillator) and K27 (suspended in a PMMA matrix.)

$$\frac{1}{\lambda_{\rm irradiated}} = \frac{1}{\lambda} + \frac{1}{\mathcal{Z}} \tag{3}$$

Since λ is unchanged, the two relevant parameters b and $\mathcal{Z}$ are easy to determine.

Reference [13] measures these parameters for a polystyrene scintillator SCSN-38 and K27 in a polymethylmethacryllate matrix. These numbers are given in table III. These numbers may be criticized as being not especially relevant to the materials which we wish to study (PVT or polystyrene scintillator with K27 in a polystyrene matrix). However, according to Ref. [12], in terms of radiation damage, PVT < PS < PMMA, where "<" implies the radiation damage is less. Thus, the numbers given in table III are worst-case estimates. In addition, by formulating the question in the form given in eq. 1, one has used the very attractive property that the radiation effects are factorized from geometrical and intrinsic ones.

Using a characteristic length in scintillator of one centimeter and an effective attenuation length of 1.1×10^{-8} cm^{-1}rad^{-1}, one finds that a dose of 100 Mrad is needed to reduce the attenuation length to one centimeter. Of more note is the intrinsic light yield decrease of 4% per Mrad. In order to decrease the light yield from the scintillator by 1%, a dose of 250 krad is necessary.

When one considers the WLS fiber, the situation is more problematic. A characteristic length is 1.5 meters. The effective attenuation length of a silvered fiber of this length is ~ 10 meters (as shown in sec. IV). The question one must answer is what radiation dose is needed to reduce the signal seen at the output end of the fiber by a specified amount. As can be seen in eq. 1, this damage will be maximized at the far end of the WLS fiber which, for this example, we take to be at $z = 1.5$ m. If one uses the maximum factor $1/\mathcal{Z} = 0.2 \times 10^{-8}$ cm^{-1}rad^{-1}, and the formula

$$R = e^{-150 \times 2 \times 10^{-9} \times D} \tag{4}$$

(where R is the deviation from non-irradiated fiber $I_{\rm irradiated}/I_{\rm non-irradiated}$, $R = 1$ implies no damage), one can determine damage as a function of the radiation dose D. It is slightly more convenient to define a parameter $\delta = 1 - R$ where $\delta = 0$ implies no change in light response. If one makes this substitution and solves eq. 4 for D, one finds

$$D = -3.33 \times 10^6 \ln(1 - \delta)$$

where D is the radiation dose in rads and δ is the fractional deviation from the non-irradiated signal. Figure 14 shows the radiation doses needed to degrade the light yield in the range of 0-10%.

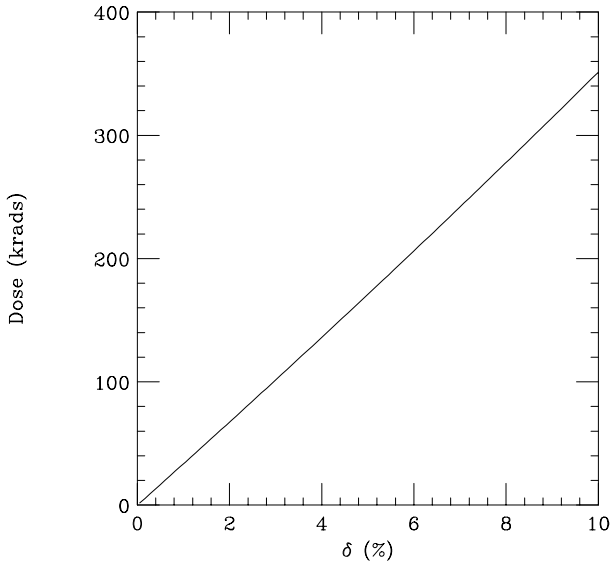

FIG. 14. This plot shows the radiation dose needed to cause a specified amount of damage. A 10% degradation requires a 350 krad dose.

So the net result is that a 50 krad dose will affect the light output by approximately 1%. As shown sec. VIII, at a total integrated luminosity of 5 fb^{-1}, the integrated preshower radiation dose is expected to be about 10 krad, which yields a negligible radiation damage to the scintillator and WLS system. Even assuming an order of magnitude error due the crudity of these calculations, we demonstrate that the preshower detector as currently conceived should have no visible radiation damage.

There is a separate consideration, which is very poorly understood. There have been initial tests [18] which suggest that scintillator which has been heated prior to radiation testing has a greater sensitivity to radiation damage than scintillator which has not been heated. In this reference, the transmission of light at 500 nm through a 1 centimeter piece of SCSN-38 scintillator was 6% worse for heated scintillator than non-heated for a 1 Mrad dose. It was much worse for 430 nm light (approaching 50%). All of the caveats mentioned above apply here. The scintillator tested has a different plastic matrix, has different fluors, and is generally quite different than the scintillator we propose to use. Nonetheless, this is a concern which we would prefer to investigate.

C. Cosmic–Ray Tests

The use of plastic scintillators to detect the passage of charged particles is now a mature technology. In the DØ upgrade, plastic scintillating fibers will constitute a substantial fraction

of the new central tracker. Each scintillating fiber will be connected by a separate plastic fiber to an individual VLPC (see sec. VII).

The DØ preshower detector must fulfill several tasks. It must function in an energy measuring mode. This is to restore the original DØ detector's electromagnetic energy resolution, which will be degraded by the presence of the magnet. It also needs to aid both in electron identification and in measuring the position that particles transit the preshower detector. In sec. III we show that the size of an electron shower in the preshower detector is on the order of a centimeter. This suggests that a detector granularity of $\lesssim 0.5$ cm is optimum. This size choice minimizes the likelihood of having unresolvable adjacent electrons (or photons) and gives one a chance at resolving somewhat overlapping electrons or photons. In addition, channel count (with its associated cost) is held to a minimum.

A substantial design restriction is the amount of space available. The preshower detector must sit between the outer wall of the magnet cryostat and the inner wall of the central calorimeter cryostat. Thus the preshower is restricted to a cylindrically shaped annulus with inner radius of 71.73 cm and an outer radius of 75.9 cm. These numbers account for the space occupied by the lead mounted on the outside of the solenoid (see sec. II).

Given the restrictions outlined above, several technologies were considered. The technology that was considered most promising was the use of scintillator strips with axial wavelength shifting fiber readout. Since the light spectrum from WLS fiber is similar to the scintillating fiber used for the central tracker, it is possible to use the same photodetector for both. This has the attractive property that the central preshower can benefit from the extensive R&D effort of the DØ central tracker group. In addition, keeping the photodetector the same opens the possibility of fast (Level 1) electron triggers using a combination of central tracker and central preshower information.

Thus it becomes imperative that this technology be tested. To this end, two cosmic ray tests were performed. The details of these tests are given elsewhere [14,15], but the results are outlined here.

1. Square Cross-section Strip

The first test [14] investigated one meter long strips of scintillator with 4.5×5.0 mm cross section (see Fig. 15). These strips were milled into large sheets of commercially available Bicron [6] BC-404A and BC-404BL scintillator. Adjacent strips were separated by injecting a white reflective epoxy in the milled slot between them. In addition, ball grooves were milled into each strip, allowing a WLS fiber to be inserted parallel to each strip's axis. These fibers were 835 μm diameter, double-clad Kuraray [7] Y-11 [16] fiber with a WLS concentration of either 250 or 350 ppm. In addition, 835 μm Bicron BCF-91A single clad fibers were tested. A total of 128 channels were available and 14 small variations on the base design were tested. Eight strips for each variant were thus tested, which allowed a measurement of the inter-strip non-uniformity of response due to construction. In addition, 16 channels were allocated for preliminary tests of a new technology where individual strips of scintillator were extruded.

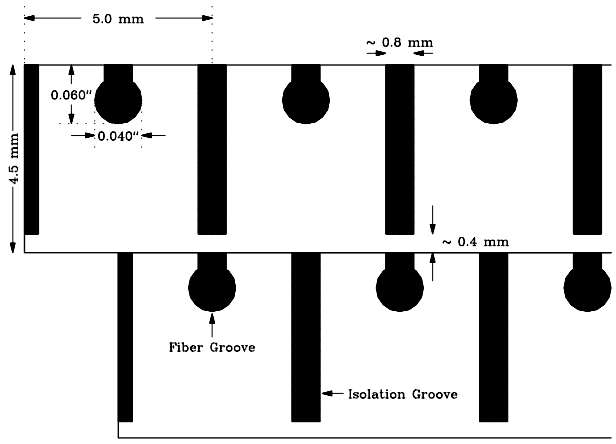

FIG. 15. Example of mega-tiles made of scintillating strips of square cross-section.

These strips were tested by allowing cosmic ray muons with a minimum energy of ∼2 GeV to pass through the prototype module. Each muon was tracked with a precision of 80 μm along the small dimension of each strip and a precision of 3.0 mm along the long dimension. Each strip was hit by approximately 15 000 separate muons. The large data set and precise tracking information allowed the response of each strip to be precisely characterized.

The first property to be discussed is the uniformity of response as a function of the position that the cosmic ray muon crosses a strip. Figure 16 shows the light yield along the long dimension of the strip, while Fig. 17 shows the response of a strip for particles crossing different positions across the short dimension of the strip. By fitting the result of Fig. 16 to an exponential $\exp(-z/\lambda_{\rm eff})$, one can determine the effective attenuation length. An effective attenuation length is different than the actual attenuation length of the WLS fiber (independently measured to be 4.5 m) because the non-readout end of the fiber has been silvered by vacuum deposition (with a measured reflection coefficient of 0.5-0.7). However $\lambda_{\rm eff}$, measured to be $\sim$ 10 meters, reflects the degree of uniformity in response that one can expect across a strip in this view and includes the effects of attenuation and reflection.

As seen in Fig. 17, the presence of the fiber groove clearly affects the uniformity of response across the strip. Three different fiber groove depths were tested (0.050", 0.060", & 0.100") and the degree of non-uniformity is related to the depth of the fiber groove. Thus a more shallow groove is preferred. In addition, the underlying cause of the non-uniformity suggests a possible solution. Because the wavelength shifting fiber does not scintillate, the signal for particles that pass through the fiber is lower. To this end, we have special ordered fiber which contains both WLS and scintillator dopants. While these fibers have not been tested as of this writing, we expect that this non-uniformity can be improved by judiciously tuning the scintillator and WLS fluor concentrations.

As seen in Fig. 15, after manufacture a small amount of scintillator remains below the isolation groove that separates adjacent strips. This scintillator provides a path whereby light generated in one strip can pass into an adjacent one. Since light undergoes many bounces within a strip, the amount of crosstalk expected is just the ratio of this small thickness of scintillator

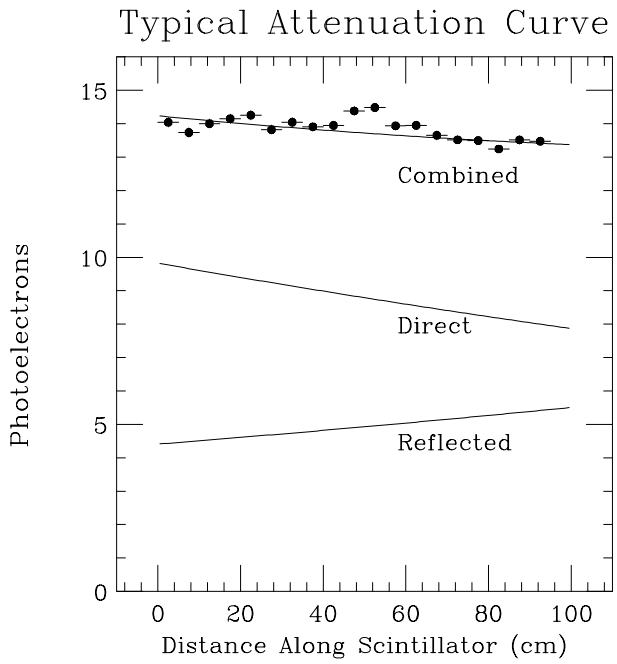

FIG. 16. Typical uniformity in response as a function of position along the long dimension of the strip. The data is given by the points, while the curves denote direct light, reflected light and their combined effect.

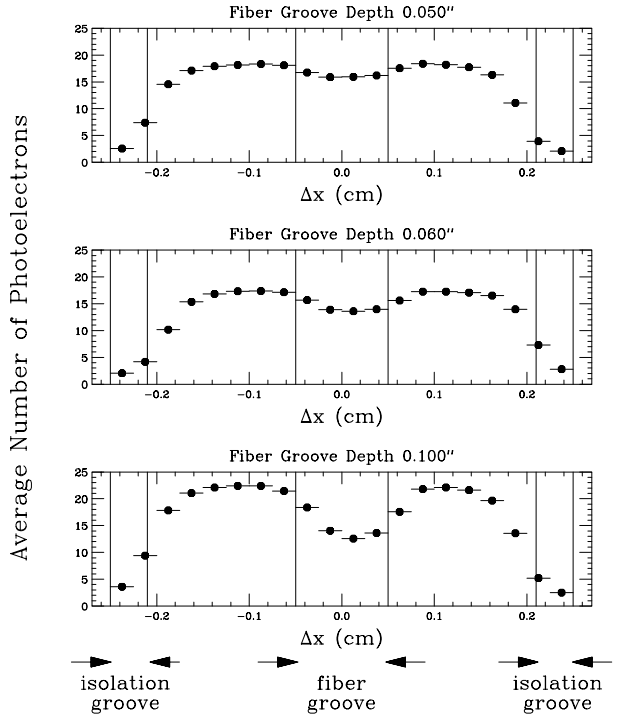

FIG. 17. Uniformity in response as a function of position across the short dimension of the strip. Each plot corresponds to a different fiber depth.

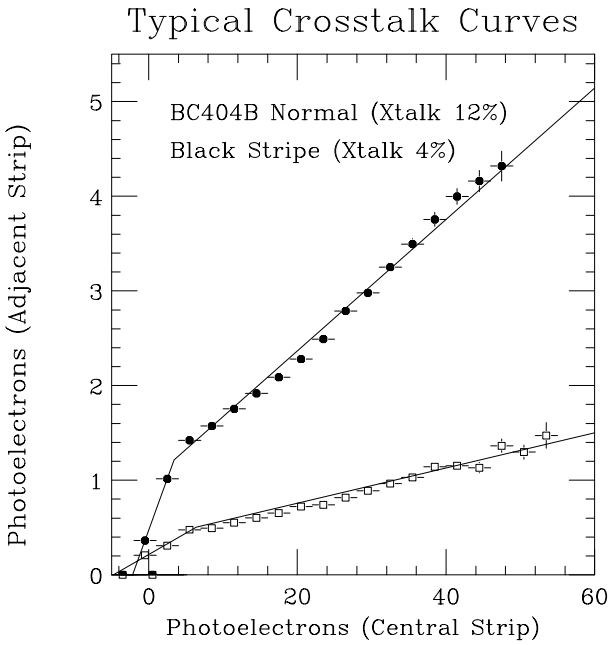

FIG. 18. Example of crosstalk curves for two different detector variants. The lower curve is the 'Black Stripe' variant, while the higher curve is the normal variant. Counter-intuitive dual slope behavior is present.

(0.015") to the total scintillator thickness (0.177") or 9%. One might expect that the amount of actual crosstalk could be measured by simply plotting the average signal observed in an adjacent strip as a function of the signal observed in the central strip, but this expectation neglects the effects of independent Poisson fluctuations of the signals in each strip. This effect is discussed in detail in Ref. [17], where a prescription for extracting the actual crosstalk from observable quantities is given. Following this prescription, we measure a crosstalk of $\sim 12\%$, in rough agreement with expectations. This amount of crosstalk is relatively large and we would prefer to reduce it. Since the light passes from one strip to another through reflection off the scintillator surface below the isolation groove, one might be able to reduce the inter-strip crosstalk by drawing a black stripe below the isolation groove. This technique was tried and an inter-strip crosstalk of 4.5% was achieved, suggesting that the presence of this black stripe is desired.

The final aspect of the strip's performance that is discussed here is the signal yield. The yield was measured by excluding tracks that pass near the strip edges or through the fiber grooves. By dividing by each strip's measured thickness, a fair comparison of each variants yield is possible. The yield is given in units of number of photoelectrons observed per millimeter of scintillator traversed. Figure 19 shows the photoelectron distribution for a particular variant. Table IV C 1 gives the yields achieved for the different detector variants. There appears to be little difference between them, with a typical photoelectron yield of 4-5 photoelectrons per millimeter of scintillator traversed. The optical glue variant's yield is higher, which is due to the fact that the space between the scintillator and the WLS fiber is filled with Bicron BC-600 optical glue, rather than the normal air. While this detector variant has a higher yield than the others, it is much more difficult to make and it is unclear if the extra signal is worth the extra

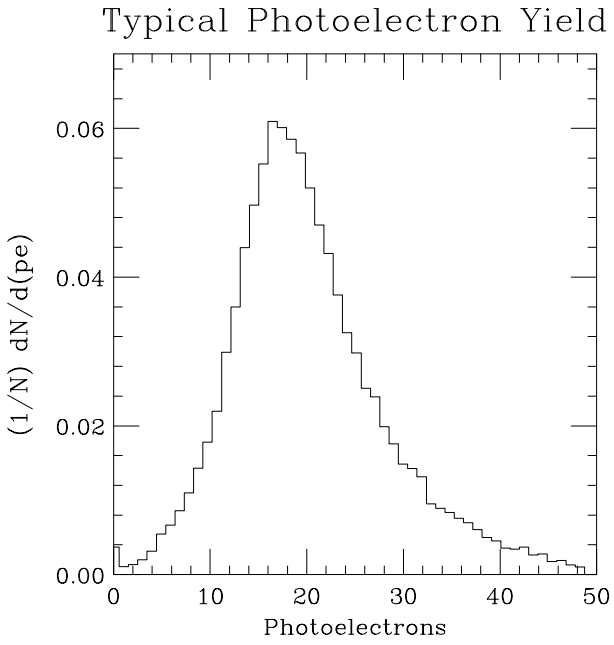

FIG. 19. Example of a typical photoelectron yield for particles crossing the maximum thickness (4.5 mm) of scintillator.

effort. In addition, the color stability of optical glue in a moderately high radiation environment is uncertain, thus adding to the reservations of using this detector variant.

Using the light yield of 4.0 photoelectrons per millimeter of scintillator traversed, with a scintillator thickness of 5 mm gives a total yield of 20 photoelectrons. In order to see minimum ionizing particles with 99.5% efficiency, a yield of 5.3 photoelectrons is needed. Electron showers typically contain many minimum ionizing particles and thus it would appear that the light yield of this technology is adequate to the task.

Because the dimensions of the scintillating strips, WLS fibers, and clear fiber light guide are nearly the same that is intended in the final design, the photoelectron yields are useful numbers. However, these yields include the light output of the scintillator/WLS apparatus, the effects of two connectors, 8 meters of clear fibers, and the quantum efficiency of the VLPC's. In the event that a different light transport and readout sequence is used, a useful number is the number of WLS photons seen at the end of the WLS fiber for each millimeter of scintillator traversed. This information is given in Table IV C 1. More details on this point can be seen in Ref. [14].

2. Triangular Cross-section Strip

A few aspects of the square strip mega-tiles give cause for concern. The first is that the white glue in the isolation grooves is optically inert and this introduces a (0.8 mm)/(4.5 mm) $\sim$ 18% inefficiency. This inefficiency can be negated with the addition of a second layer of

square strips, offset by half a cell. However, the need for this extra layer doubles the channel count and perhaps more importantly doubles the necessary radial space budget.

A second consequence of the square design is that the position resolution of minimum ionizing particles for each strip of width a is simply $a/\sqrt{12}$. In addition, because no interpolation is possible, the position of the particle is reported simply as the center of the strip. An improved position resolution might be desired for certain measurements.

Both of the above concerns can be addressed through the use of strips of a different cross-section. A mega-tile consisting of interlocking triangular strips is shown in Fig. 20. The lack of a dead region for normally incident particles is manifest and it is apparent that one may use the ratio of signals in adjacent strips to interpolate the position that isolated, normally incident minimum ionizing particles cross them.

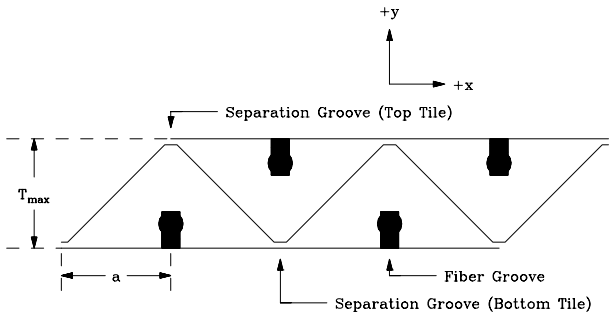

FIG. 20. Example of mega-tiles made of scintillating strips of triangular cross-section.

A second cosmic ray test was done to test this new detector variant. These results are given in Ref. [15]. Many of the measurements discussed above were repeated for this test (e.g. effective attenuation length, $\lambda_{\rm eff}$) with similar results. We therefore discuss only those results unique to this test.

If one were to measure the distance a cosmic ray passes from the long axis of the strip and plot the photoelectron yield as a function of this variable, one would expect a triangularly shaped distribution. The presence of the fiber groove would cause deviations from this expectation. A plot of this form is shown in Fig. 21. As expected, the effect of the fiber groove is observed. Although not shown here, the depth of the fiber groove is related to the degree to which the yield uniformity deviates from a triangular function. This suggests that a shallow fiber groove is desired.

The yield is determined by fitting the data in fig 21 to a triangular function, restricting the fit to the region indicated in the plot. Table V lists the achieved yields in units of photoelectrons per millimeter of scintillator traversed. We see that yields of 3.5-4.0 pe/mm are common, somewhat less than that seen with the square strips. This discrepancy is explained as due to surface effects. In the case of squares, half of the surface area was covered by reflective white glue; the remaining surfaces were smooth and covered with Tyvek. In the case of triangular strips, two surfaces were milled and somewhat milky in appearance. The third surface was smooth. All three surfaces were covered with aluminum foil. As seen in Table V the triangular strip variant with white painted sides has a higher photoelectron yield than other variants.

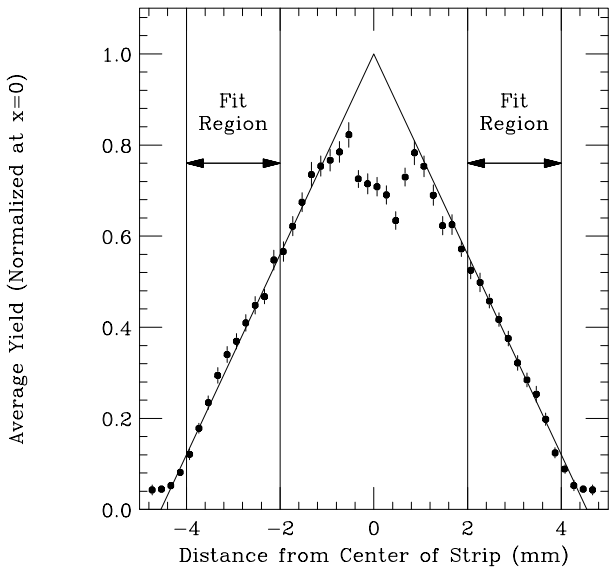

FIG. 21. Example of the response of triangularly cross-sectioned strips as a function of the distance a cosmic ray passes from the axis of the strip.

This suggests that white painted surfaces are desired.

The inter-strip crosstalk was determined much in the same way as discussed for square cross-section strips. The amount of crosstalk is tabulated in Table VI. The expected amount of crosstalk is predicted as discussed previously. In most cases, the observed amount of crosstalk is larger than predicted. One likely explanation for this behavior is that the aluminum foil wrapping the strips is insufficiently tight and allows more inter-strip light transfer than the simple model suggests. This explanation is further supported by the crosstalk observed for painted strips, which is nearly equal to expectations. This result further supports the idea that the triangularly shaped strips should be painted. Adding a black stripe as was done in the case of square strips may further reduce crosstalk.

Another aspect of the triangular mega-tiles that has proven to be important is the inter-tile alignment. The position at which a particle crosses two adjacent strips can be given as

$$x_{\rm vernier} = x_o \pm a \frac{S_2/S_2^{\rm max}}{S_1/S_1^{\rm max} + S_2/S_2^{\rm max}} \tag{5}$$

where x_o is the position of strip 1, $2a$ is the length of the base of a triangle, S_1 and S_2 are the signals in strips 1 and 2 respectively and $S_1^{\rm max}$ and $S_2^{\rm max}$ are normalization constants. This equation assumes normally incident charged particles and further assumes that the center of strip 1 is exactly at x_o and that the center of strip 2 is exactly at $x_o \pm a$. However, as discussed in Ref. [15], the top and bottom tiles within a mega-tile are not always positioned exactly as desired. This changes equation (5) slightly. This effect can be corrected for and Fig. 22a shows the position reported by two adjacent strips (using a small variation of eq. (5)) as compared to the position reported by a precise tracker. No systematic shifts are observed. Figure 22b shows the distribution of residuals of these two measurements. A position resolution of 567μm

is achieved. Prior to correcting for the small inter-tile shifts, position resolutions of 700-1000μm were observed, underscoring the need for precise inter-tile alignments.

3. Analysis

While both strip cross sections have been shown to perform adequately for the needs of the DØ central preshower detector, the triangular strips are superior. The lack of dead space, reduced radial space usage and reduced channel count make them the clear choice. Although the extrusion triangular strips have not been tested using cosmic rays, we expect that the light yield should be very similar to that of the machined strips. Since the decision to use the extruded triangular strips has been made, we will pursue the mechanical design for this option. For the WLS fiber, both multi-clad Y11 and Bicron single-clad BCF-91A fibers are adequate for achieving the performance of the preshower detector. Although the as-yet-untested Bicron hybrid fiber should improve the non–uniformity in the detector response, it is unlikely that the fibers will be used for the preshower detector given the tight schedule. Nevertheless, we plan to complete the R&D of the hybrid fibers. We will make a decision between Kuraray multi-clad and Bicron single-clad fibers in January pending detailed comparisons of the other properties of the fibers.

V. STRIP GEOMETRY AND MECHANICAL ASSEMBLY

As is apparent from the discussions in Sec. III, a number of different designs have been considered. Ultimately, the choice of extruded strips of triangular cross-section was made, as was the decision to have 3 layers—one with strips oriented parallel to the beam (axial strips), the other two oriented at angles near $\pm 20^\circ$ with respect to the beam (stereo strips). In order to facilitate construction, each layer will be subdivided into eight "octants".

A. Strip Dimensions

Ref. [15] suggests that position resolution is related to photoelectron yield which, in turn, is related to the thickness of the scintillator. Using a triangle base of 9 mm, a height of 4.5 mm and a photoelectron yield of ~ 4.0 photoelectrons per millimeter of scintillator traversed, a position resolution of 560 μm for normally-incident minimum ionizing particles has been achieved. Monte Carlo studies have shown that a detector constructed of scintillating strips with this intrinsic MIP response will have a position resolution of 1.4 mm for electrons with 10 GeV of transverse energy. Ref. [15] also shows that for small variations in the photoelectron yield (in the operating region achieved in the test stand, i.e. 18 photoelectrons per MIP) even smaller changes in the resolution are obtained. Thus increasing the thickness of the strip does not substantially improve the resolution and we therefore assign a strip thickness of 5.5 mm as the maximum that we will likely want to use.

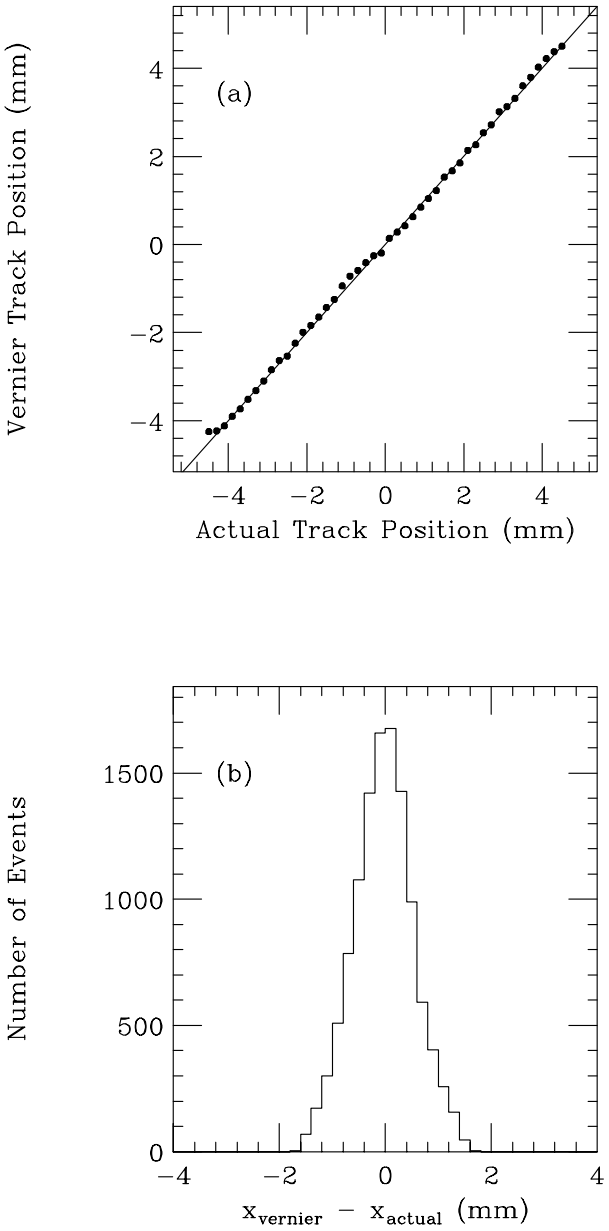

FIG. 22. (a) The position reported by the prototype module as a function of actual impact position of the charged particle, after accounting for the inter-tile shift. The superimposed line denotes a perfect correlation. (b) Distribution of residuals after the inter-tile shift correction.

The transverse strip dimension is chosen in order to cover the full azimuth. The layer of axial strips will be part of the Level 1 trigger, essentially as an additional layer of the fiber tracker. The central tracker will be split into 80 sectors, each of which will be assigned to an individual VLPC cassette containing 1024 channels. In each VLPC cassette, 32 channels are allocated for VLPC use. As of this writing, it is thought that a single WLS fiber will be used per strip, requiring only 16 channels per sector. With 80 sectors per axial layer, this implies 1280 channels in the axial layer. However, a second option is a choice where each strip will contain two fibers that are half as long as the strip. These fibers will meet at $z = 0$ and be read out independently on opposite sides of the detector. This design reduces the strip occupancy by a factor of 2, although it doubles the number of VLPC channels needed by the preshower. However, since the preshower is allowed 32 channels per axial sector, this design is still acceptable and can probably be used at little or no extra cost.

The outer diameter of the solenoid is nominally 70.78 cm. The lead wrapping and cooling volumes are allocated 0.95 cm of space. Thus the preshower volume begins at a radius of 71.73 cm. Assuming 5.5 mm thick scintillator, surrounded by two 1/16" thick aluminum skins, a preshower layer is ~ 8.5 mm thick. Thus each layer is assigned a 1 cm thick radial annulus, with the intent that each layer is centered on that space.

In order to ensure that the detector will fit together, one must leave a small tolerance between adjacent octants. Leaving such a 1 mm space implies that 8 mm of the circumference is not occupied by the detector. The inner radius of the axial scintillator is then $71.73 + 0.50 - 0.55/2 = 71.955$ cm, with an outer radius of 72.505 cm. The circumference is then $2\pi(71.955) - 0.8 = 451.307$ cm. Finally, this leads to a fiber-to-fiber spacing of 0.3526 cm and a triangle base of 0.7052 cm.

The strip length is determined by the length of the solenoid and the need for space for the connectors. The solenoid is 273 cm long. If the preshower is 250 cm long, 11.5 cm is left on each end for the connectors and fiber routing. This length means an $|\eta|$ coverage up to 1.32.

Depending on construction techniques, there is another consideration that must be remembered. The inner radius and outer radius of a particular layer of scintillator is not the same. This implies that neither is the circumference. For the axial layers, the outer circumference (excluding the inter-octant separation) is $2\pi(72.505) - 0.8 = 454.706$ cm. The fiber-to-fiber spacing is then 0.3553 cm, with a triangle base of 0.7106 cm. When one compares with the inner circumference of the same layer, we find that each triangle must be 54 μm wider for the outer radius than the inner radius. Converting to inches, one finds the differential size increase is 0.0021". Such a small increase does not necessitate a separate triangular cross section shape, but it does require a small change in the inter-triangle spacing. This question only becomes relevant if a top and bottom layer are made separately (i.e. the extrusion are effectively made into tiles, which are combined into a megatile). If a bottom layer is made and then the upper strips are laid in by hand, then this question is no longer a consideration.

The stereo layers are more problematic. Two obvious questions must be answered: (1) What are the implications of using the same size strips? and (2) What will simplify the mounting?

Answering the first question is straight-forward. If one wishes to keep the octant structure without cracks and to have a stereo angle $\sim 20°$, then the question is entirely constrained. The

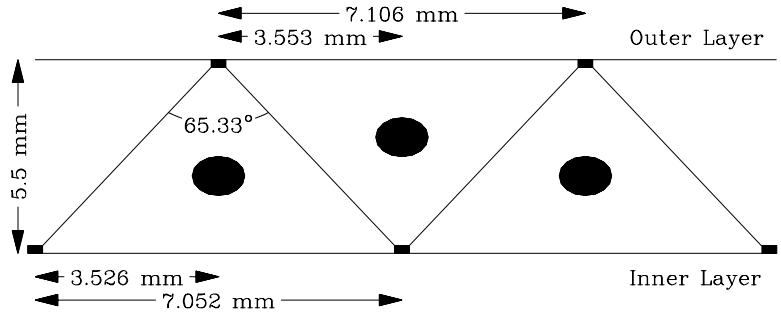

FIG. 23. Shown is the proposed dimensions of the axial strips. The difference in the dimensions of the inner and outer layers is highlighted.

inner radius of the inner stereo layer is 72.955 cm, while the inner radius of the outer stereo layer is 73.955 cm. After calculating the circumference, subtracting the inter-octant tolerances, and separating into octants, one finds an octant arclength of 57.199 cm and 57.984 cm respectively. Each octant must contain an even number of strips (which is less than 160, the number of axial strips in an octant). After experimentation, one finds that the choice of 150 strips per octant implies a fiber spacing, projected along the end of the axial cylinder of 0.3813 and 0.3865 cm respectively. As suggested by Fig. 24, this corresponds to stereo angles 22.37° and 24.18° for the inner and outer stereo layers. Table VII lists the relevant strip dimensions and parameters for this design choice.

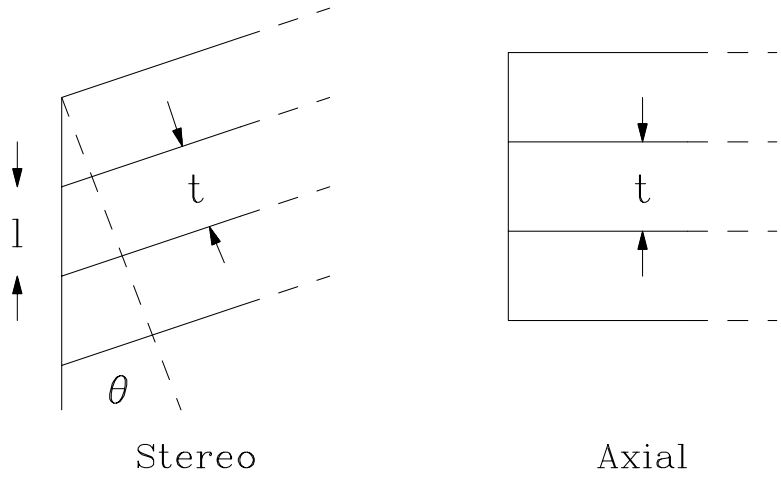

FIG. 24. Shown is a schematic of the stereo angle calculation. If the thickness of the strips t is kept the same for both the axial and stereo layers, then the stereo angle is determined by the projection of the stereo strips along the axial projection l. This quantity l is calculated by requiring an integer number of stereo strips around the circumference.

While such a design is attractive due to the fact that it uses only strips of a particular cross-section, it necessarily is more difficult to mount. Mounting is simpler if all layers, stereo and axial, could be mounted from a single fixture (c.f. Fig. 25). One way to easily accomplish this is to require that the edges of the stereo modules align with the axial modules (see Fig. 26). Using the octant arclength calculations given above, along with the solenoid length of 273 cm,

yields an inner and outer stereo angle of 22.73° and 23.02°. However, this choice requires strips of different dimensions. Some latitude is possible in how the new dimensions are calculated, but assuming that the 160 strips per octant structure is preserved, this requires a strip base of 0.6594 and 0.6671 cm for the inner and outer stereo layer. The difference in these two triangle bases is 77 μm. It is likely that a single design of the stereo strip will be sufficient, and the small additional fiber to fiber separation can be achieved by changing the separation between strips during construction. Table VIII lists the relevant strip dimensions and parameters for this design choice.

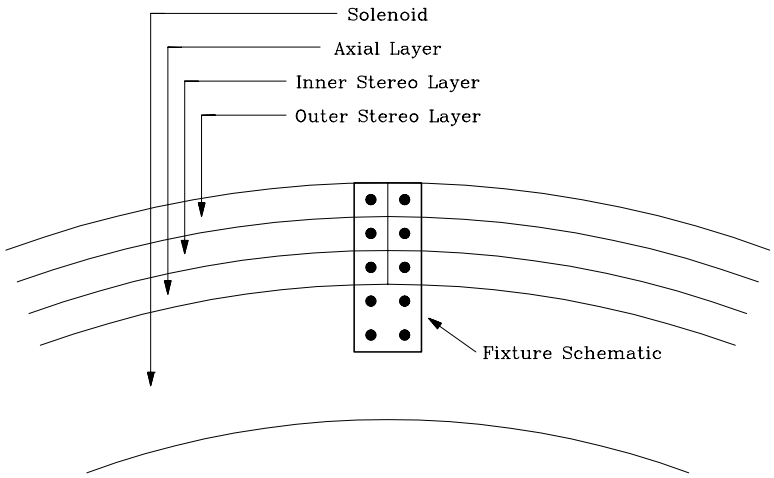

FIG. 25. Shown is an example of how a single mounting fixture can support and align all layers. The filled in circles denote something which serves the same purpose as a bolt and/or alignment ball. The break between adjacent octants within a layer is shown.

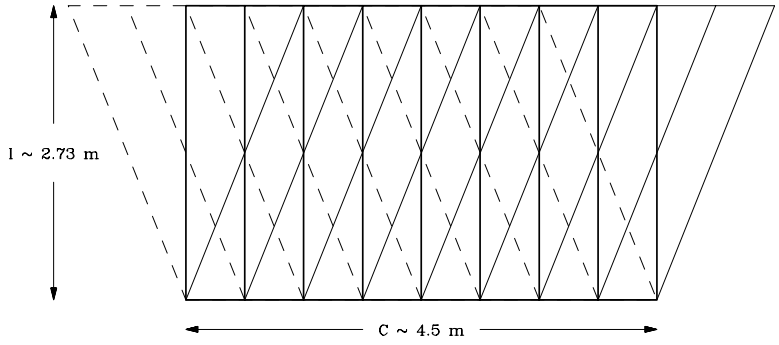

FIG. 26. Shown is the central preshower, unwrapped in a plane. Note that the stereo octant edges are precisely aligned with the axial octant edges.

B. Preparation of Parts

1. Strip Wrapping

The scintillator strips are wrapped in Aluminized Mylar using the wrapping machine in IB3. The machine can proccess about 3.5 ft/min of stock. We will wrap 1700 10 ft strips and 3400 12 ft strips for the axial and sterreo layers respectively. This totals 57800 ft, which gives 16500 minutes, or 275 hours. Assuming a 40 hour week, this means 6.8 weeks of wrapping are required. The wrapping machine requires two technicians to operate. One operator has to be skilled in the operation and tuning of the machine. The second operator has to only minor tasks.

2. Slumping Press

The triangular strips are slumped to the required helical shape. This relieves stresses in the plastic and makes assembly easier. The axial strips are also slumped to make them straight, (the strips tend to bow after extrusion and wrapping. Five distinct shapes are required for the CPS. The axial layer requires only straight strips. The stereo layers each require two distinct shapes. These are labeled as the top and bottom layers. The top and bottom shapes for the inner and outer stereo layers are non-interchangeable.

The strips are slumped with the aid of a slumping press, (fig X). This device holds the strips to the desired shape. The press and strips are then warmed to 180 deg F for 1 hour followed by a slow cool. The device is being built to fit into the large oven and lab 8. The basic design of the press is shown in (fig X). Two Al skins surround a .25" layer of teflon. The teflon has triangular grooves milled in. The teflon is then rolled to the desired radius and held in place between the skins. After the strips are heated and cooled, the press will be used to cut the strips to length and to do final proccessing on the exposed ends. Cutting to length is done by sliding all the strips out one edge of the press. A circular saw can then cut off the exposed ends. A guide for the saw will be installed on the press. Using a measured rod, the strips are all slid back into the press until the opposite ends are exposed. These are then cut as before. It is expected that accuracy of 1/16" can be easily achieved. Note also that a .002" thick piece of tape must be placed on each strip before cutting to hold the wrapping in place. Following the final circular saw cut, white paint will be applied to the exposed scintillator at the end of each strip. The paint can be sprayed or applied with a small sponge. After the paint dries, the fiber holes will be beveled using a dremel or hand held drill. This has two purposes, to clear the fiber hole of paint and plastic left there during sawing, and to facilitate insertion of fibers during assembly and also if fibers/connectors need to be swapped out after installation.

The production model press will be capable of holding 50 strips in each stereo layer and 100 strips in the axial layer. The production proccess, as currently envisioned, plans for one heating cylce per day. At this rate, approximately 19 days are required to proccess the planned 5700 strips.

3. Al Skin Fabrication

The Al skins will be fabricated off site by one of several local machine shops. The specific grade/type of Al is planned as 6160 t6 mill finished. While the skin is still flat, the desired final dimensions are marked. The Al is then rolled to the desired radius of curvature, +- .5". Note also the sheets tend to be less curved in the middle than at the ends. Following the rolling, the skin is slid into a powered shear. Two technichians on either side of the shear align the marks on the skin to the edge of the shear and hold the skin in place during cutting. The cut on the stereo skins is done by flattening the skin to the shear table and cutting. Stereo skins have been made from 48" square Al sheets and the procedure is straight forward.

4. Assembly Tables

Three special assembly tables are being built for the manufacture of the CPS modules. The top of each table is a cylindrical surface corresponding to the radius of each of the three CPS layers. One octant at a time will be assembled on each table. The axial table will have dimensions 119",33",5.5" (l,w,h) and have 34" of arclength. The stereo tables need to be bigger, having dimensions, 119",60",28" with approximately 78" of arclength. The tables have approximately 12" more arclength than needed to accomodate a single octant panel. This to accomodate manufacturing procedures, (covered below). Several types of alignment pins will be located on the tables. These are used in aligning various pieces of the CPS modules during assembly. The specific functions of these pins is covered in the next section. The assembly of the tables, and the method of locating holes, (for the alignment pins), on the table surface are discussed next.

The requirements of the table design are,

1. Provide a smooth cylindrical surface of accurate radius of curvature. 2. Position alignment pins accurately, minimizing systematic and random errors. 3. Accomodate manufacture techniques. Several main issues are that during the vacuum bagging procedure the table does not leak excessively, that it be rigid enough to not deform when glue applied during assembly, and that the surface of the table be accessable to technicians, (important for stereo tables).

The design presented below has evoled from the above considerations and construction of a prototype table.

The cylindrical surface is formed from 1/8" Al, mounted to 3/4" phenolic ribs. The phenolic ribs are machinined to the proper radius at lab 8. The Al skin is rolled beforehand, and then takes on the radius of the phenolic ribs. The error on the radius of curvature of the ribs is .001". The surface of the table will be assembled from seven 17" wide Al skins. Before rolling, holes for the alignment pins, and for securing to the ribs will be placed in the skins by a CNC milling machine. The Al skins are not mounted directly to the phenolic. Instead a .125" by 2" Al strip is mounted to the top of the phenolic rib. This provides .625" of overhanging material. In the overhang, an oversize hole is drilled. A flat head screw goes into the Al skin, through the oversize hole, and is secured with a locknut, (see Fig XX). The oversized holes in the overhang

are to account for mounting errors, phi and z, in the Al strip. The error in r, due to mounting the strip to the phenolic is ¡¡.005". In order to align the Al skins relative to one another The Al skins are tightened to the Al strips

C. Assembly Procedure

A cross sectinal view of a completed module is shown in fig X. Important features to note are: 1. the Al skin does not extend to the edge of the module. 2. The last strips on either side have opposite orrientation.

The basic assembly procedure for each octant is showm schematically in figures x,x,and x. The first step is to place the inner skin on the assembly table, aligning it to the "false strip" fixture. This fixture is placed over the alignment pins and is thus well positioned. A thin (.003") layer of epoxy is applied to the inner skin. To speed this operation, the glue will be applied in beads from air powered syringes. This glue will then be smeared into a thin, uniform layer with either a roller or squeegee. The bottom layer of 80 strips is then added. About five strips at a time are put in place. A hand held alignment jig aligns these strips to the "false strip". This is done for for each small group of strips to avoid having to move all 80 strips at once on the tacky glue. When all of the strips are in place and roughed into position by hand, the grooved alignment jig is placed over top. This assembly is then vacuum bagged to provide a uniform force over the entire area. On the following day, when the glue is dry, the top layer is added, using the bottom layer as a guide. Glue is added inbetween each triangle, again using air powered syringes. A modified squeegee with triangular teeth cut into it is used to smear the glue in the groove evenly. At this stage the mounting blocks and fiberguide are also glued to the inner skin. The mounting blocks and fiber guide need to be positioned acurately with respect to the strips. There will be special holes milled into the assembly table into which go alignmnet pins to position the mount blocks and fiber guide. The mounting blocks and fiber guide are in the prototype stage so the exact specifics of this arrangement have not been worked out, although it is straight forward. Fig X shows a strawman arrangement. Note that the Top skin is not yet added, instead thina thin piece of teflon is placed overtop, followed by the felt pad and vacuum bagging material. Again this is allowed to dry. The next day, the fibers/connectors are added. At this point source testing will be done. Upon successfull source testing, the final skin can be glued on. This is again vacuum bagged overnight. Some final fting out will be done to the mount blocks to strengthen thier bond to the Al. This consists of either spotwelding or drilling and tapping holes for round head screws.

VI. CONNECTORS AND LIGHTGUIDE BUNDLES

A. Connectors

1. Background

In the preshower detector, fiber-to-fiber connectors are needed to transport the light to remote VLPC's. The connectors should have reproducible light transmission greater than 95% and be made so that the assembly of the connectors could be done efficiently and easily. The University of Illinois at Chicago (UIC) developed v-groove connectors and has done extensive research in fiber connection as described in detail in two conference records [22,23]. The work is outlined as follows.

While the initial effort was directed toward the scintillating-fiber tracker, the results are also applicable to the preshower detector. A total of eight connector pairs were assembled and tested during the process of improving the connector performance. In the beginning, prototype 128-channel v-groove connectors were machined from black Delrin plastic. After initial assembly with fibers and before gluing, the front face of each connector was wrapped with a clear plastic sheet to prevent glue from flowing down. The connector was then clamped into a precision parallel clamp with the front surface facing down. Multiclad fibers are difficult to glue because the fluorinated polymer comprising the outer cladding is a smooth, Teflon-like material. A variety of epoxy adhesives were tested to see which is suitable for attaching the fiber to the Delrin connectors [24]. Based on the results of the investigation, BC-600 epoxy supplied by Bicron [6] was chosen because of its high strength and because it is formulated for gluing plastic scintillator. After injecting the BC-600 epoxy from the back end of connectors, it cured overnight. Then the connector was placed in a clamping jig and inserted into a special diamond fly-cut tool designed and made at Fermilab [25]. The tool has its own microprocessor that controls cycles of rough cuts and final cuts. It took about eight minutes to finish one connector.

Two pairs of connectors, one-to-one type (0.965-mm-diameter fiber to 0.965-mm-diameter fiber) and step-up type (0.835-mm-diameter fiber to 0.965-mm-diameter fiber), were made by machining Delrin plastic resulted in excellent average light transmission. Immediately after assembly, using optical grease [26] at the joint, the transmission was measured to be $98\pm2\%$. The measured light transmission for the one-to-one connector assembly is shown as a sample in Fig. 27. Based on Fresnel's reflection formula, the maximum transmission for an ideal connection, with optical grease that has refractive index 1.40, is about 99%. Both one-to-one and step-up connector pairs had almost the same high values of average light transmission. So a design without step-up from wavelength shifting fiber to clear lightguide fiber became a possible choice. To date, the two machined connector pairs have kept their values of average light transmission greater than 95% for a one year period.

An injection molding machine was installed in the UIC machine shop to make connector bodies by injection molding rather than machining for fast and reliable production. Initial attempts to make Delrin plastic connectors using the injection molding machine were unsuccessful,

because the thermal shrinkage after molding of about 2% was not reproducible. Acrylonitrile-butadiene- styrene (ABS) plastic was found to shrink only about 0.5% and showed better reproducibility. One connector pair was successfully made of ABS plastic by injection molding. The two alignment pin holes were drilled after molding. Transmission measurement for the injection–molded connector assembly yielded an average of 95% when it was assembled using optical grease as the couplant. This slightly lower transmission is believed to be caused by a small misalignment in the connector pair assembly, since the alignment pin holes were drilled after injection molding. No essential differences were noticed between the transmission properties of the machined and the injection–molded connectors.

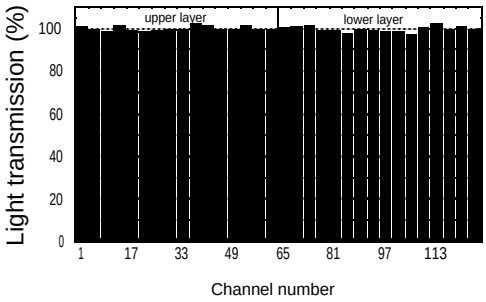

FIG. 27. Measured light transmission for a connector assembly of the one-to-one type (0.965-mm-diameter fiber to 0.965-mm-diameter fiber) assembled using optical grease as an optical couplant.

There are several effects that contribute to the lessening of light transmission in connectors. Axial misalignment is a major source of light loss. For the 0.965-mm-diameter fibers having a 1 mil (25 microns) misalignment at the connector joint, the ratio of the overlapped area to the full cross-sectional area is 0.967, resulting in a light loss of about 3.3%. To achieve light transmission greater than 95%, the misalignment must be held to less than 1.5 mils or 38 microns. Angular misalignment was not found to be a serious problem in the multichannel connectors. A variation in the fiber diameter of 1% at the joint gives a light loss of about 2%. Because fiber makers such as Kuraray [7] are able to control the variation in fiber diameter within one per cent, this should not be a big problem. Fiber end surface roughness is not a problem because we use a diamond fly-cut tool [25] for the faces. Gap size must be minimized and a proper optical couplant be placed in the gap. Using a simple setup including two micrometers, we measured that the light transmission between two 0.965-mm-diameter fibers decreases linearly by about 2% for every mil increase of the air gap size up to a gap of 0.5 mm. Using Fresnel's reflection formula at the connector gap interface, we calculated for a polystyrene fiber core with index of refraction 1.59 a transmission of 90% through air and 99% through optical grease having an index of refraction of 1.40.

A search for a non-fluid optical couplant such as index-matching film made of silicone rubber is underway. In a temperature-controlled environment, optical grease works well as a couplant, and is preferred to mineral oil [27] because of its higher viscosity. Mineral oil, being less viscous, flows away from the fiber joints more easily. Several different optical couplants were tried at the interface of fiber-to-fiber connectors. The results of the study are as follows. With no

optical couplant except air between the mating connector faces, the average transmission was $12 \pm 3\%$ less than the perfect joint as measured with the control fibers. It is consistent with a value of about 10% expected from Fresnel's reflection formula. Light loss using optical grease was only $1 \pm 1.3\%$ immediately after assembly, and the value after one year is about 2% higher. Mineral oil worked as well as the optical grease immediately after assembly, but the transmission dropped some 5% within a few days due to the flow of the low viscosity oil. A 1-mil-thick index matching film made of silicone rubber [28] had losses of $2 \pm 2\%$. A few other different silicone rubber films were tried but seemed to transmit somewhat less light than optical grease. One measurement using a 2-mil-thick film made of silicone rubber from ACE hardware store [29] gave $2.5 \pm 1\%$ loss.

Stability of light transmission through the connector pairs has been monitored. The values of average light transmission over a period of one year were better than our goal of 95% for the two machined connector pairs, as shown in Fig. 28. The minor variations are believed to be caused by the flowing of optical grease due to variation of the ambient temperature. The room temperature has been checked when measuring the connectors. The room temperature varied in a range between 18 C and 25 C for the period of one year. The injection–molded connector pair, assembled using the 2-mil-thick ACE silicone rubber film, has also been monitored. As shown in Fig. 28, its light transmission has been stable for eight months to within $\pm$ 1%, although the connector assembly has the fixed misalignment that corresponds to a light loss of about 4%.

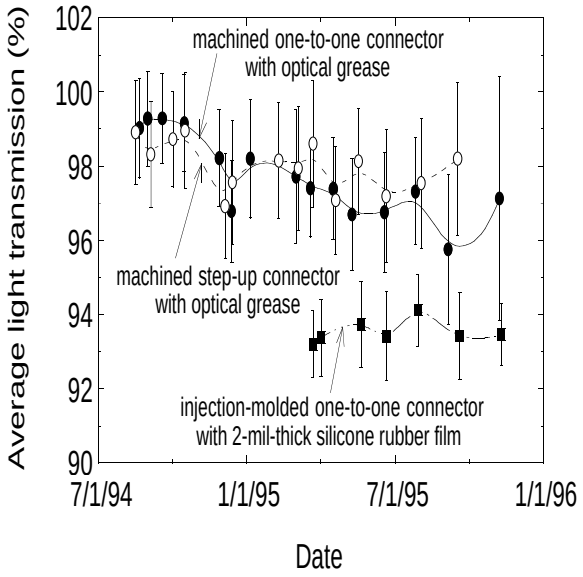

FIG. 28. Long-term stability of light transmission through connector assemblies.

In the current design of preshower detector, a 16-channel connector at the detector end is a good match to the 16-channel connector at the VLPC cassette end proposed by Carl Lindenmeyer at Fermilab. This connector is to be cast directly on the fibers at room temperature.

A 16-channel prototype "holed-connector" is shown in Fig. 29. It is $4 \times 6 \times 42$ mm. Several pairs of the connector were made at the UIC machine shop by injection molding from black ABS plastic. Three pairs using Kuraray multiclad clear fibers of 0.835–mm–diameter were assembled. Two of them had S–type fibers and the third one had non-S type fibers. Using optical grease as an optical couplant, an average of $(91 \pm 4)\%$ light transmission was measured. (Fig. 30 gives the results for a connector assembly having S–type fibers).

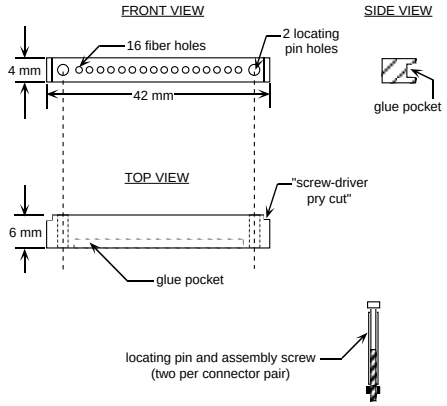

FIG. 29. Schematic drawing of a 16-channel connector designed to be placed at the end of the triangular scintillator strips.

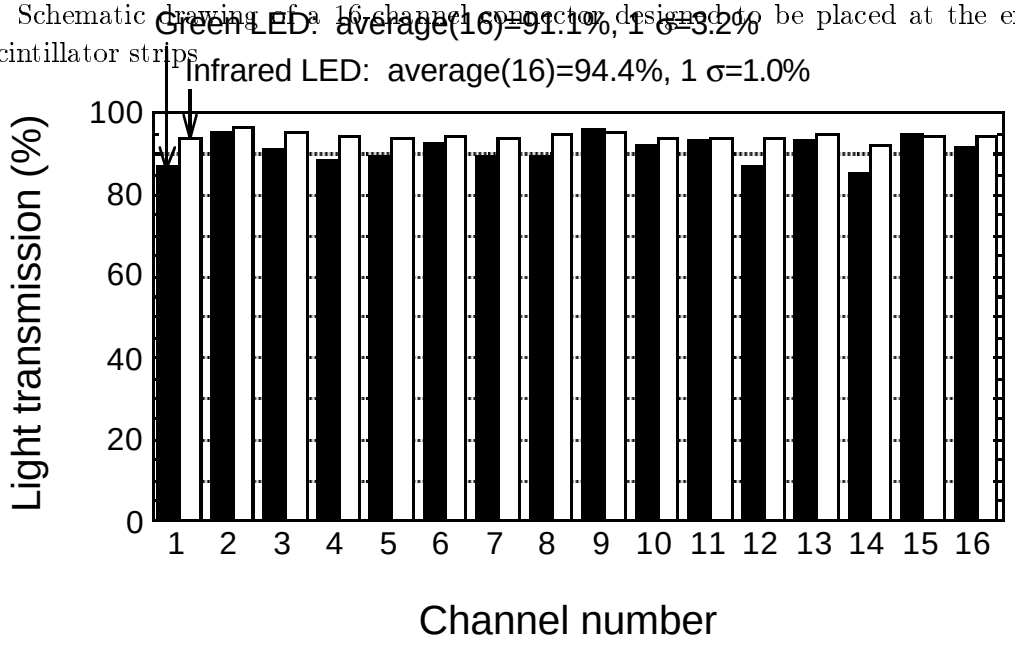

FIG. 30. Light transmission measured using a green LED and an infrared LED through the prototype connector assembly having S type fibers.

A green LED was used in all of our previous connector measurements. Lately we found that an infrared LED is useful in understanding the light transmission through a connector assembly, especially in evaluating the fiber-to-fiber matching. By employing the infrared LED for several connector assemblies, the average values of light transmission increased by up to 4the values measured using the green LED. The connector assembly with almost perfect light transmission shown in the previous section (Fig. 27) resulted in the same perfect transmission with the infrared LED.

The infrared LED has a peak wavelength at 880 nm, while the green LED is peaked at 565 nm. Based on a preliminary study with the infrared LED, the transmission of the green light is affected by the following factors possibly due to its short wavelength: (1) The non-S type fiber loses about 2light than the S–type fiber in making a fiber–to–fiber connection; (2) Finishing by using the diamond fly–cut tool depends on the connector body material. Connectors made of Delrin plastic had the best light transmission and others such as ABS plastic, polyurethane, and aluminum lose 2(3) The connectors assembled with 0.835-mm-diameter fibers have a loss of at least 2% more than the connectors assembled with 0.965–mm–diameter fibers. The infrared light eliminated most of the discrepancies and gives more information on the connector assembly. However, a measurement using the green light should also be made because it represents the value in the real detector.

By using the infrared LED as a light source, the average value of light transmission of the prototype preshower connectors reached at $(94 \pm 2)\%$. There is a possibility of increasing transmission by 3% by replacing the pins for the fiber holes used in the mold. The pins were gauge pins with a diameter of 0.889 mm (0.035"). Assuming a shrinkage of 0.5% of ABS plastic after injection molding, the inner diameter of the holes is estimated to be around 0.885 mm. It is 0.05 mm (0.002") bigger than the fiber outer diameter, perhaps explaining the estimated loss of about 3%. Pins with a diameter of 0.859 mm (0.0338") are being used to make a new mold. The fiber holes will be about 0.855 mm, which will leave a tolerance of 0.020 mm for the 0.835–mm–diameter fiber allowing a variation of $\pm 1\%$.

In order to save space particularly for the chimney from the superconducting magnet and other supporting structures, it was suggested to have a connector smaller in width. The new design is $4 \times 6 \times 19$ mm in size (as shown in Fig. 31) having 16 holes arranged in a zigzag pattern to make 2×16 channels. As described above, the pins for the fiber holes are 0.859 mm in diameter. The connector has a pocket for gluing the fibers and "screw–driver pry cuts" at the short edges of the mating faces for use when prying open the joint. Two mating connectors will be assembled using the two locating pins that have tapped holes for assembly screws. The two locating pins are different in diameter to give an asymmetry for correct matching in fiber channels. They have a round head with a cut to match a keyhole made in the detector–side connector. A proper optical couplant, such as a thin layer of optical grease or possibly of silicone rubber film, will be placed at the connector joint for index matching.

The lightguide–side connector does not have the keyholes with everything else the same as the detector-side connector. After a lightguide–side connector, a plastic boot (as shown in Fig. 32) wraps a group of 16 fibers in a lightguide bundle. The boot will reduce strain and protect fibers from ambient light.

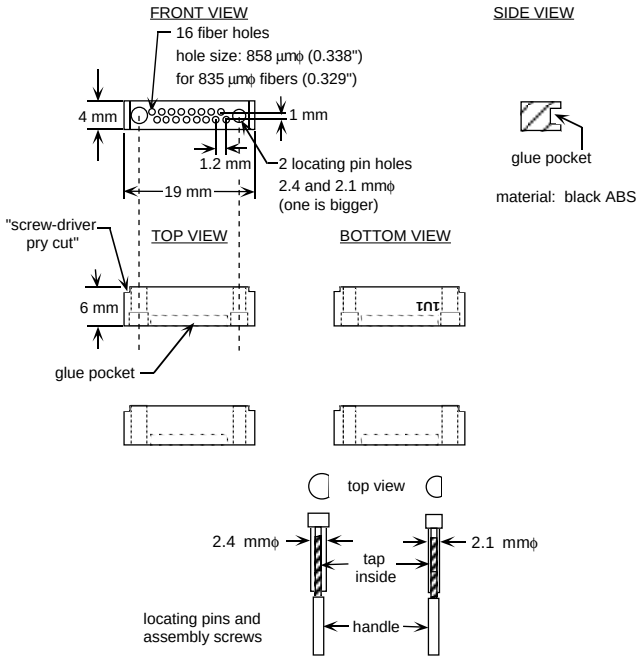

FIG. 31. Schematic drawing of the new 16-channel connector designed to be placed at the end of the triangular scintillator strips.

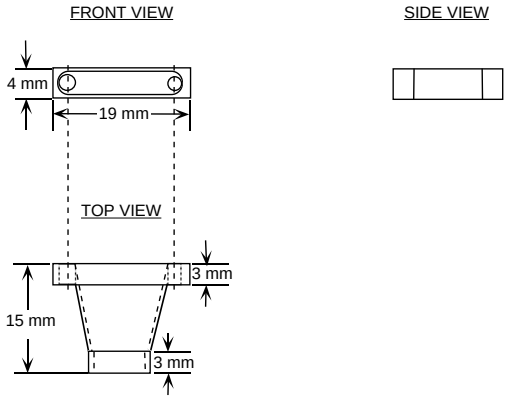

FIG. 32. Schematic drawing of the boot for the preshower connector.

Since the connector will be connected to the scintillator/substrate assembly by very flimsy WLS fibers, an additional mechanical assembly is needed. For each connector, a special shroud will be made. The shroud will consist of a block of opaque plastic with channels milled out for each fiber. These channels will run from each strip to the connector. The connector will be held firmly in the shroud assembly. Further a cover will be put on top of the shroud in order to facilitate light-tightness. This shroud will be placed between the two skins that surround the scintillator and held in place by either double-sided tape or a small mechanical assembly. It is possible that for each channel that contains an individual fiber, a blue-emitting LED can be mounted for quick tests of the photodetection system. See Fig. 33.

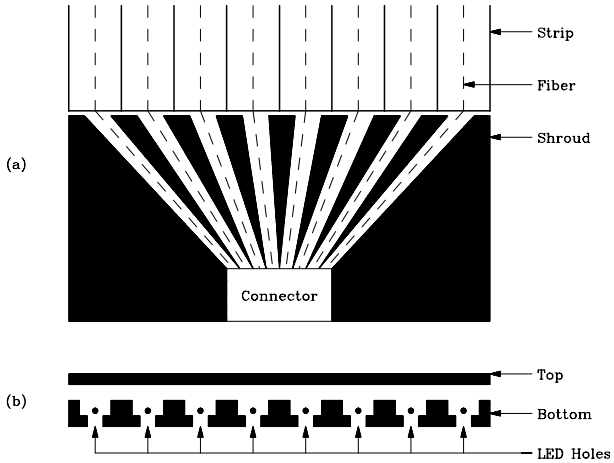

FIG. 33. (a) A stylized view of the shroud. The fibers follow channels in the shroud from the strips to the connector. In reality, the channels will be curved and there will be 16 channels/connector. (b) An end-on view of a slice of the shroud. The top and bottom parts of the shroud are shown, as well as holes for blue LED's.

B. Lightguide Bundles

1. Background

As a part of the fiber tracking collaboration, UIC made 30 128-channel lightguide bundles, either 8 m or 11 m long, employing some 20 miles of fiber. Twenty four of them have been successfully used in the cosmic-ray test setup installed at Fermilab Lab 6. Each of the bundles was made with two 128-channel holed square-shape connectors made by machining from black Delrin plastic. The details of the bundle fabrication can be found in Ref. [30].

As in the lightguide bundles already made, multiclad clear fibers made by Kuraray [7] will be used in the lightguide bundles to carry scintillation light to the VLPC's. These fibers consist of an undoped polystyrene core enclosed by two concentric layers of cladding. The inner layer is made of acrylic plastic, the outer of a fluorinated polymer; the wall thicknesses are each about 25 microns. The advantage of these fibers over standard single-acrylic-clad fibers results

from the fact that the refractive index of the fluorinated polymer (1.42) is lower than that of acrylic (1.49), producing a larger total internal reflection light-capture cone and thus a considerably brighter fiber. The inner acrylic cladding layer is required because the fluorinated polymer adheres poorly to polystyrene but well to acrylic plastic. In addition, multiclad clear fibers have longer attenuation lengths of about 10 m [31] and are mechanically more robust that single-clad fibers. Kuraray makes two different types of fiber from exactly the same base material. They are called "non-S type" and "S type". The conventional non-S type fiber is known to have attenuation length about 30% longer than the S type fiber, but the non-S type is more brittle than the S type. For bundle making, the S type fiber is preferred because it is easier to handle for its flexibility. Recent results on connector measurements have shown that the fiber-to-fiber connector joint for the non-S type fiber seems to lose more light (up to several %) than the S type fiber connector joint does. Therefore, the multiclad clear fiber of the S type manufactured by Kuraray is the best candidate for the future fiber lightguides.

The old bundle making process is briefly described here. Bundle fabrication began by inserting a pair of degreased connectors in their holders. Then, an appropriate length of fiber was unwound from the fiber spool and cleaned with ethyl alcohol using lint-free wipes. After all connector holes were filled, the connectors were removed from their holders and inserted into another pair of fixtures for epoxying. These fixtures held the connectors in a horizontal plane with the fibers emerging vertically. For gluing ends of lightguide fibers in the connectors, Bicron BC-600 epoxy was used because of its high strength and because it is specially formulated for gluing plastic fibers [24]. After allowing the epoxy to cure for about 24 hours, the fibers were enclosed in a black PVC jacket manufactured by the Zippertubing Co [32]. The jacket served to protect the fibers and keep them physically together. To reduce the likelihood of breaking fibers at the connectors due to handling, aluminum strain reliefs were attached at both ends. After construction of the fiber bundles was completed, all connector faces were polished on a special facing machine employing a diamond-tipped fly-cut tool that was dubbed "P-3" at Fermilab [25].

Each of the bundles fabricated was tested for light transmission, both to validate the fabrication procedure and to check the quality of the Kuraray fiber. Excluding one bundle that appeared to be damaged in handling, the bad channel frequency was found to be 0.2% for all 3712 channels of 29 lightguide bundles. The light loss per channel resulting from insertion of a bundle and its two connectors was measured to be about 5 dB for 8-m-long bundles. It is consistent with a clear fiber attenuation length of 10 m and a transmission efficiency of about 90% per connector joint.

The results of these measurements validate the design and construction procedure used, and it is expected that similar and advanced procedure will be employed in fabricating clear lightguide fiber bundles for the preshower detector as well as the scintillating-fiber tracker.

2. Sixteen-channel Lightguide Bundles

The preshower detector will have 16-channel clear lightguide fiber bundles as unit bundles. The cassette end of the bundle will have the 16-channel cassette-end connector that will mate

with the warm-end connector on the VLPC cassette top. The other end of the bundle will have an appropriate 16-channel connector made for the preshower detector.

Sixteen-channel lightguide bundles will be made using the following steps. Using the light-guide bundle maker that is described in the next section, 16 pieces of fiber of appropriate length of tentatively 11 m are cut one by one with both ends marked for continuity of channels. After grouping 16 fibers, each end of the bundle will be placed into a black plastic sleeve of about 1 m long for protection and keeping light-tight. Both ends of the bundle will have the sleeves. Then, fiber ends will be stuffed into holes of connectors in correct order on both ends. Then the ends of the bundle will be glued into the connectors.

Four such 16-channel bundles will be grouped together and be enclosed by 3/8" diameter black PVC jacket manufactured by the Zippertubing Co [32]. A strain relief will be assembled at each end. Strain relief on the cassette-end connector is designed as a cast boot, and strain relief on the detector end will be injection–molded from a black plastic material. The strain reliefs protect fibers from damage during handling and keep the fibers light-tight. The four 16-channel connectors will be placed in a clamp for diamond fly-cutting.

3. Lightguide Bundle Maker

The UIC machine shop is currently making a lightguide bundle maker employing a motorized fiber pulling system. The objective of the bundle maker is to allow for various cable lengths, from 8 m to 11 m with each fiber having the same length. It will be used extensively for the 256-channel lightguide bundles for the scintillating fiber tracker and it can also be used to make the 16-channel bundles for the preshower detector. One person is needed to assemble the cables and they will have access to both ends at the same time. Fibers will be pulled out and cut into the necessary lengths. Both ends will be placed in a holding jig that including the actual connector or the connector mold for the cassette-end connector. After stuffing 16 fibers, the ends will be cut with the flat face of a single-wedge blade so that tests of continuity and light transmission can be performed before gluing as described in the next section. A screen display driven by a master program in a Pentium PC will remind the operator which bundle and fiber are being worked on. The same program will record the transmission and continuity results and do the bookkeeping on all the bundles. After initial assembly, the ends of the fibers within the connectors have to be glued. After gluing, the connector ends will be faced using a diamond fly-cut tool and the bundles will be retested for their final light transmission.

Figure 34 shows schematically the initial design of the lightguide bundle maker. Currently the wheel and belt system has been made and installed on a frame. Experimentation and adjustment need to be done on every part in the design. The followings are the main features of the bundle maker. The fiber spool is placed horizontally and a tension adjustment is made to keep the feed smooth. The fiber will pass through a belt guide and a cleaner pad soaked in ethyl alcohol. An affordable laser gauge system is being searched for use to check fiber diameter continuously during fiber pulling. Two small fiber clamp assemblies are fused to the belt. The end of the fiber is attached to one clamp and is pulled around the belt. The fiber will be held by friction on the belt. Once the fiber has come around, the motor pulling the fiber is stopped.

The fiber is attached to the second clamp to establish the length and then cut. The tension on the pulley is relaxed momentarily and the fiber falls off the pulley and into split PVC pipe troughs. The operator takes one end at a time and places the ends into connector setups. After four groups of 16 fibers are installed, tests are made on continuity and light transmission. Any mistake detected in the tests will be corrected and fiber with significantly low light transmission that loses 20% or more compared to normal fibers will be checked and replaced if necessary. Adjustment of bundle length will be made by moving the two front wheels. The belt needs to be changed to the length when the length adjustment is made.

We have a room to have just the right size and shape for the bundle maker as shown in Fig. 35. The total length of the device is about 5 meters and, at its widest, the width is 5 meters. There is enough room for the computer and other electronics in the corner of the room.

4. Estimation of Man-hours for Bundle Fabrication

For a single length bundle, pulling, cutting, and placing in the end holders of 16 fibers we estimate about half an hour, including the time to put them into two black sleeves and cut off the ends. For four such bundles, the testing for continuity and light transmission will take about one hour. The gluing of the fibers to the connectors is overnight. The facing off of the ends requires about one hour per set of four 16-channel bundles. Testing the final connections should take about one hour per set of four 16-channel bundles. The total time to assemble four 16-channel bundles is as follows:

We will require the equivalent of two full time people who could complete 28 16-channel bundles a week at best. For a total of about 480 16-channel lightguide bundles we need about 17 weeks or four months. This number of channels is needed for the design option where the WLS fibers are split at $z = 0$. The baseline, single-WLS-fiber, design will take about half as long.

5. Test and Quality Control

A multi-channel fiber tester is being made employing a PC. To help in developing an automatic fiber bundle tester, a 16-channel prototype tester was made and tested to be functioning properly. Light sources selected are green LED bargraph unit, with which we studied light output as a function of applied voltage and light output as a function of time. A phototransistor was chosen as light detectors because it can be used in a simple dc mode without an amplifier. The program in the prototype testing was written in Quick BASIC version 4.5. The multi-channel tester will include a 16-channel analogue-to-digital converter (ADC), analog multiplexers and LabView by National Instruments and it will test a lightguide bundle of up to 256 channels of fiber at a time. The setup is schematically shown in Fig. 36.

Quality control is important in making reliable bundles with fewer bad channels. A preliminary check before gluing is essential to screen bad channels and any human mistake before it

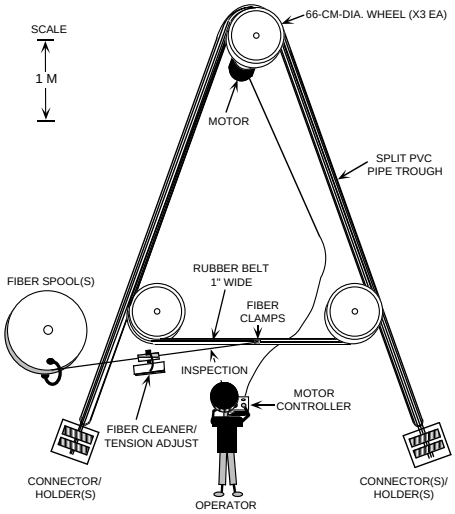

FIG. 34. Schematic drawing of the lightguide bundle maker.

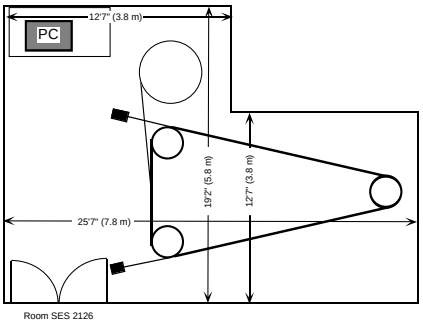

FIG. 35. Room 2126 in science-and-engineering-south (SES) building at UIC is assigned for the lightguide bundle maker.

is too late. It includes a sequence check to confirm correct continuity and a measurement of light transmission to find out bad fiber and replace by a good one. We studied fiber end finish by using a few different knife blades. We found that the flat face of a single-wedge blade gives better fiber-end surface, resulting more light transmission. By using 100 pieces of 36-cm-long 0.965-mm-diameter Kuraray multiclad S-type clear fiber, we measured light transmission of 77±4% by cutting both ends of fibers using the single-wedge blade as compared to 100% for fibers with both ends cut using a single-fiber diamond fly-cut tool [25], while the normal razor blade of the double-wedge type resulted only 33%±12%.

The final test of each bundle will be made after gluing and surface finishing with a diamond fly-cut tool for connectors. The continuity is checked again for confirmation and bookkeeping. Light transmission through all channels will be measured and channel-to-channel variation will be calculated. This will allow to find any bad channel that transmit light less than 80% of normal channels. Absolute comparison between bundles will be made by keeping a few control bundles and measuring them for comparison with the bundles being produced.

To control the quality of the bundles, attenuation lengths of different batches of fibers will be monitored by making one set of fibers with lengths of 1 m, 3 m, 5 m, 10 m, 15 m, and 20 m for each incoming batch of fiber spools with the frequency of about one set of fibers every few months. They will be used to estimate attenuation length of the fibers and also to understand the fiber-to-fiber variation. By measuring the sets of fibers once every few months, any possible long-term fiber aging will also be followed.

Computer programs will be written for production control and bookkeeping. The programs are required to make and update listings of the incoming fiber spools, various connectors, produced lightguide bundles, and their test results. Each produced bundle will have tags attached explaining its brief history and test results.

VII. READOUT SYSTEM

A. Dynamic Range

The dynamic range needed for the readout system is set by the energy deposited in the preshower strips by low and high p_T electrons. The distributions of maximum single–strip energy deposition by $E_T = 10$, 50 and 100 GeV electrons are shown in Fig. 37. While 100 GeV electrons deposit a large amount energy in the preshower detector, the energy deposited by 10 GeV electrons is as low as a few MIP's. Ideally, a range of 1–300 MIP will be needed to be sufficiently sensitive to both low and high p_T electrons. However, studies show that saturation above 50 MIP has little effect on the position and energy resolution of the electromagnetic shower. Taking into account a factor of two differences in response due to the angle effect, a dynamic range of 1–100 MIP is specified for the readout system. This range should be adequate for both low and high p_T electrons from b–quark and W/Z decays.

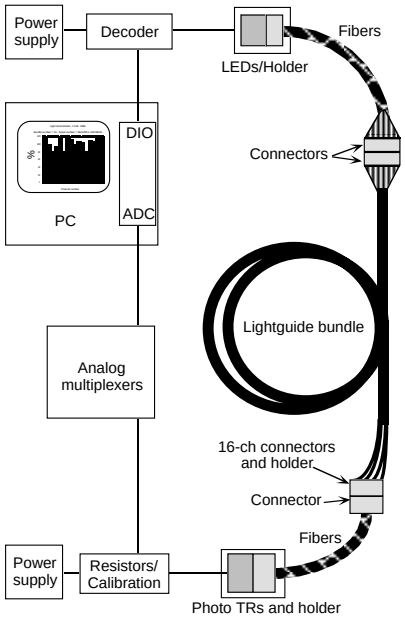

FIG. 36. Schematic drawing of the lightguide bundle tester.

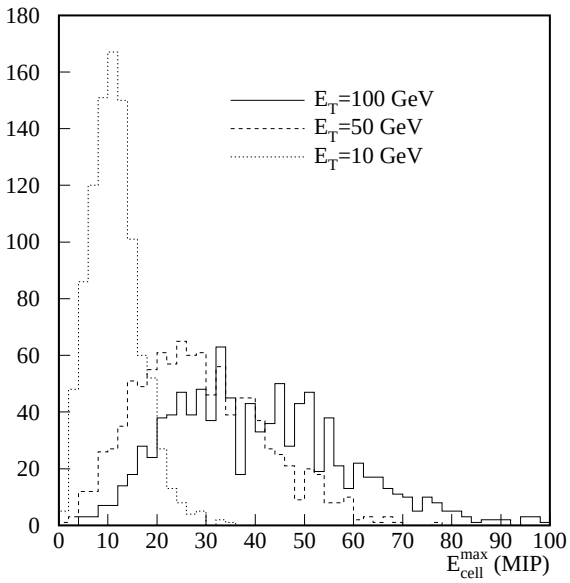

FIG. 37. The distributions of the maximum preshower single–strip energy deposited by $E_T = 5, 10, 50, 100$ GeV electrons.

B. Visible Light Photon Counters

Photodetectors of high quantum efficiency, high gain and high rate performance are required to detect minimum ionizing particles for the fiber tracker readout. Photomultipliers are not well suited due to their low quantum efficiency and the presence of the magnetic field. The DØ collaboration has undertaken extensive studies of VLPC's under development at the Rockwell International Science Center. VLPC's will be used as photodetectors for the scintillating fiber tracker. Given the similarity between the preshower detector and the scintillating fiber tracker, the VLPC's become the natural choice for the preshower detector. In addition, the use of VLPC's will enable the preshower and the scintillating fiber detector to share the same electronics cards, which is essential for the Level–1 electron trigger. This solid state device is capable of high–rate, single photon counting with a quantum efficiency greater than 70% at a wavelength 550 nm. Typically, the VLPC has a gain of about 10^4 at an operating voltage of 7–8 volts. The VLPC's will have to be operated at a temperature around 6–8 K, requiring a helium cryogenic system. A great deal of progress towards the development of such a system has been made in DØ, as summarized in Ref. [4].

The scintillating fiber tracker needs only to be sensitive to MIP–like particles while the preshower detector must be sensitive to electromagnetic showers over a wide energy range. Dynamic range and high rate capability of the VLPC's are issues need to be addressed for the preshower readout. Studies [21] show that the VLPC has a linear response up to 600 photoelectrons and saturates at about 10^4 photoelectrons. Assuming a yield of 15 p.e./MIP, the VLPC's have a linear response to at least 60 MIP's and saturates at about 10^3 MIP's. Therefore, the dynamic range does not appear to be a problem. However, the high rate capability of the VLPC's is a potential problem to be addressed. When an avalanche is generated in the VLPC, it deadens a small region of the VLPC pixel for a time on the order of 1 ms as quoted by Ref. [21]. If this number is true, it has significant impact on the operation of the preshower detector. As discussed in sec. III, on average about 5% of the strips will register 1 MIP energy deposition for each minimum bias event. At a luminosity of $2 \times 10^{32}\text{cm}^{-2}\text{s}^{-1}$ and assuming an total cross section of 50 mb, each strip will register an energy deposition equivalent to that deposited by 500 MIP's. For a light yield of 15 p.e./MIP, the energy deposition in a single strip in 1 ms corresponds to 7500 photoelectrons. With this large number of photoelectrons, the response of the VLPC is very non–linear [21]. The non-linearity itself does not constitute a problem provided that it can be calibrated. However, the non–linearity in this case is a serious problem since it results from the pile–ups from many beam crossings and depends on the instantaneous luminosity. This is clearly a problem need to be addressed. Note that this could also be a problem for the fiber tracker at high rate. Therefore, it is extremely important to study the high rate capability of the VLPC's.

While the fiber tracker only needs to detect minimum ionizing particles, the preshower detector must be sensitive to both minimum ionizing particles and high energy electrons/photons. To take into account this important functional difference, we propose an independent bias voltage supply for the VLPC's of the preshower detector. This configuration will give us the flexibility to change VLPC gain (and therefore the dynamic range) without interfering the operation of the fiber tracker.

C. Readout Electronics

The Level–1 electron trigger using the tracking system and the preshower detector requires a readout system for the preshower to be similar to the fiber tracking system. These considerations lead us to adopt the SVX–II chip, currently being developed at Fermilab, as the readout electronics for both the fiber tracking and preshower detector systems. The SVX–II chip functions as a preamplifier, an 8–bit ADC and a multiplexer. As discussed above, a dynamic range of 100 MIP is needed in order to be sensitive to minimum ionization particles as well as to high energy electrons. This implies 2 counts/MIP for an 8–bit ADC in the SVX–II chip. Obviously, this is too coarse for minimum ionization particles. Moreover, the SVX–II chip uses a multiplexing scheme to deal with the large number of channels, and is not suited for trigger purposes since the Level–1 trigger system needs a fast output signal from each scintillating strip.

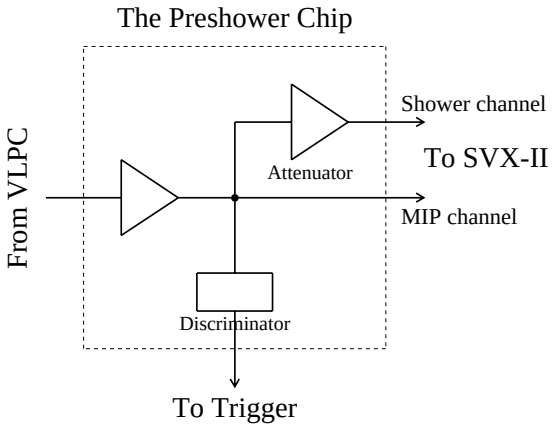

FIG. 38. Block diagram of the special chip for the preshower readout. About a factor of 20 is needed for the attenuator. With this chip, the detector will be sensitive to both minimum ionizing particles and high energy electrons/photons.

To solve the above two problems, a special chip with bilinear readout will be developed for the preshower readout. The preshower chip should contain a signal splitter, an amplifier and a discriminator that provides a fast trigger signal for each VLPC channel. A block diagram drawing of the chip is shown in Fig. 38. The two bilinear channels will be designed to be sensitive to minimum ionization particles (the MIP channel) and high energy electrons (the shower channel) respectively. Since the preshower and the fiber tracker will share the same VLPC cassettes for the trigger channels, the VLPC operation condition will be set based on the MIP response of the fiber tracker. Assuming the fiber tracker is sensitive to signals corresponding to 5 MIP's, a factor of 20 reduction in the signal for the shower channel is needed in order to achieve the desired 100 MIP dynamic range. In this design, the number of ADC counts will be 50/MIP for the MIP channel and 2 counts/MIP for the shower channel. The preshower chip combined with the SVX–II chip has the equivalent function of an 12–bit ADC and is sufficiently sensitive to both high energy electrons and minimum ionization particles. The stereo layers will be readout using the same scheme although a Level–1 trigger pick-off is not needed.

VIII. OTHER ISSUES

A. Calibration

As with all detectors, in order to have physical significance, one must convert a signal to real-world units. In order to do this, one must excite the detector with a known, stable source and observe the signal. We propose two *in situ* calibrations using the collider data. The *in situ* calibrations will allow us to take into account any possible time–dependent effect of the light yield. The first method is to use the minimum ionizing particles. Monte Carlo simulation shows that the preshower detector will be showered by the non–interacting charged pions. Figure 39 shows the single–strip hit energy distribution (in units of MIP) for $t\bar{t}$ events. The simulation was done for the square geometry and no selection requirement was applied on the hits. The peak corresponding to the dE/dx energy loss of the minimum ionizing particles is clearly visible. Therefore, the detector can be calibrated using the MIP energy loss if the readout system is capable of detecting the MIP peak. Such an intent underscores the need for a good MIP response of the readout system. The other method is to using the ϕ symmetry of physics events. No known physics will produce energy flow asymmetry in ϕ for unpolarized $\bar{p}p$ beams. It implies that any non–uniformity of the detector response can be calibrated by comparing the energy distributions for each channel. Although this method does not provide absolute calibration, it is nevertheless sufficient for calibrating a sampling component of the calorimeter.

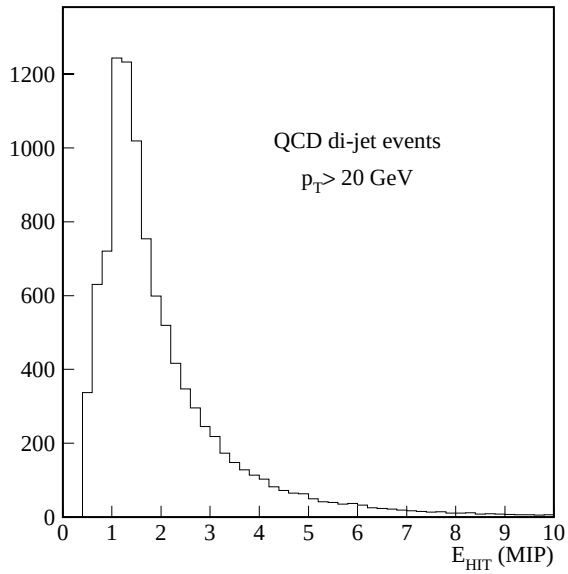

FIG. 39. The hit energy distribution in the unit of MIP for QCD dijet events for the square geometry. The peak is due to the dE/dx loss of the non–interacting charged pions.

In addition, a quick "check" would be useful. One way to do this is to use blue LED's (recently available). This light will be absorbed by the WLS and re-emitted. LED's are notori-

ously unstable and thus this technology will not measure scale or accurately measure stability. However, they do make the test: "Is the detector alive?"

Other options include the use of an ultraviolet laser. However, this option requires a separate quartz fiber, each carrying ultraviolet light to an individual channel. This greatly complicates the design and therefore is not being considered.

B. Temperature

The central preshower detector is sandwiched between two cryostats, that of the solenoid magnet and that of the central calorimeter. Although it is not anticipated that a substantial heat leak into the cryostat walls would be present, the potential exists for temperature gradients in this limited space. Temperature is not an important factor in the operation of scintillator per se, but undue temperature swings could crack the epoxies used in the manufacturing of the detector. This in turn may cause delamination of the aluminum/scintillator/aluminum sandwich. In addition, the presence of condensate on the scintillator and wave shifter fibers could modify their transmission characteristics. And, ice formation from this condensate could cause structural damage to the scintillator and the mechanical assembly.

In order to safeguard against undesired temperature swings, and water condensation, the inner surface of the central preshower will be ribbed axially, allowing this region to be flushed with dry nitrogen at room temperature. In order to monitor the temperature in this region, it is envisioned that a small number of temperature sensors would be placed throughout the preshower assembly. A reasonable number would be two per octant over one layer. These would be taped or epoxied in place. The readout system would be through the standard 1553 scheme now used to monitor DØ temperature sensors.

C. Radiation Dose Estimation

Albedo neutrons from the calorimeter, charged and neutral hadrons from the $\bar{p}p$ interactions are the sources of the radiation in the preshower detector.

The calorimeter bore is filled with albedo neutrons which are fairly homogeneous in the bore. The logarithmic energy spectrum peaks roughly around 1 MeV. The estimated neutron flux density is $\phi_n = 1.2 \times 10^4$ cm^{-2}s^{-1} at a luminosity of $\mathcal{L} = 10^{32}$ cm^{-2}s^{-1}. Using a conversion factor of 1 neutron/cm^2 $= 1.8 \times 10^{-9}$ rad, the dose rate from neutrons is given by $\frac{dD_n}{dt} = 2.2 \times 10^{-5}$ rad/s.

Assuming a minimum bias event cross section 50 mb and 4 charged particles per unit of pseudorapidity, the charged particle flux at a radius is $\phi_\pm = 3.2 \times 10^6/(r_\perp/1\text{cm})^2$ cm^{-2}s^{-1}. Taking into a factor of two for low p_T loopers, the dose rate from the charged particles is given by $\frac{dD_\pm}{dt} = \phi_\pm \times \frac{1}{\rho}\frac{dE}{dx} = \frac{0.2}{(r_\perp/1\text{ cm})^2}$ rad/s.

Most neutral hadrons are π^0's and have an average p_T of 0.5 MeV. From isospin symmetry,

the π^0 flux is expected to be half of the flux for charged particles. Assuming each photon from π^0 decay cascades to 4 electrons in the solenoid and the lead, the expected dose rate from neutral hadrons is $\frac{dD_0}{dt} = 4\phi_{\pm}(\frac{1}{\rho}\frac{dE}{dx}) = \frac{0.6}{(r_{\perp}/1\ \mathrm{cm})^2}$ rad/s.

Adding the rates from neutron, charged and neutral hadrons together, the total dose rate at $\mathcal{L} = 10^{32}\ \mathrm{cm}^{-2}\mathrm{s}^{-1}$ is $\frac{dD}{dt} = 2.2 \times 10^{-5} + \frac{0.8}{(r_{\perp}/1\ \mathrm{cm})^2}$ rad/s. The total radiation dose for the central preshower detector ($r_{\perp} = 72$ cm) is shown in Figure 40 as a function of integrated luminosity. The detailed calculation can be found in Ref. [33]. The expected radiation level for an expected integrated luminosity of 2 fb^{-1} is well below the level at which the scintillators or the fibers are affected (see sec. IV). Therefore, the effects of radiation damage on the central preshower detector is small.

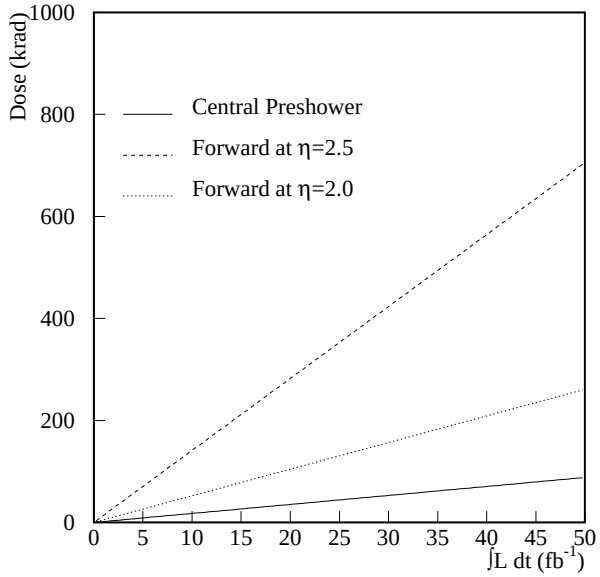

FIG. 40. The estimated total radiation dosage in the central preshower detector as functions of integrated luminosity. Also shown are the expected dosage for the forward preshower at $\eta = 2.0$ and 2.5.

IX. SCHEDULE & PLAN

The schedule of the preshower detector is dictated by that of the solenoid. The limited space between the solenoid and the calorimeter implies that the preshower detector will have to be installed on the solenoid before it can be moved into the calorimeter bore. Since the solenoid is expected to be installed sometime in 1997, the construction of the preshower detector will have to completed by the end of 1996. With these constraints, we propose the following milestones for the construction of the preshower detector.

Scintillator & fiber procurements	1/96 – 4/96
Parts preparation (jig, scintillator/fiber processing)	1/96 – 6/96
First fully assembled prototype module	– 6/96
Assembly of axial and stereo modules	6/96 – 12/96

Since the schedule for the construction of the clear–fiber bundles, implementation of the readout and of the Level–1 trigger system and many other tasks are not limited by that of the solenoid, we will concentrate on the detector construction in 1996. Materials needed for scintillator extrusion have been ordered and are expected to be ready for extrusion by end of April. The order for WLS fibers has been placed and are expected to arrive by early May. Mechanical parts for a full–scale prototype module are also being ordered. Overall, the procurements are schedule.

Within the central preshower group, the responsibilities will be shared as follows. The University of Michigan group will assume overall responsibility of the project. The Michigan group will be responsible for the detector construction, installation, commissioning and operation. The development of the fiber connectors and clear–fiber bundles will be tasks of the UIC group. While the scintillating strips and WLS fibers will be prepared at Fermilab, the final assembly and test of the modules will be done at the University of Michigan. To monitor and control the quality of the assembled modules, we plan to check every channel using a radiative source and characterize randomly selected channels using the cosmic rays. A cosmic–ray test stand with photomultiplier readout and Labview DAQ system is being setup at the University of Michigan for this purpose. We will draw assistance from undergraduate students for the construction and quality control/monitoring.

We are aware that the proposed schedule for the detector construction is very aggressive. However, we are confident that we can meet the challenge provided that we are approved for the construction now.

REFERENCES

[1] DØ Collaboration, S. Abachi *et al.*, Phys. Rev. Lett. **74** (1995) 2632.

[2] DØ Collaboration, S. Abachi *et al.*, Nucl. Instrum. and Meth. **A338** (1994) 185.

[3] DØ Collaboration, S. Abachi *et al.*, *"The DØ Upgrade"*, DØnote #2542 (1995) unpublished.

[4] D. Adams et al., FERMILAB-Conf-94/318-E, presented at DPF'94; M. Atac et al., Nucl. Instr. and Meth. A 314 (1992) 56; M.D. Petroff and M.G. Stapelblock, IEEE Trans. Nucl. Sci. **NS-36** (1989) 158; M.D. Petroff and M. Atac, ibid., p. 163.

[5] ISAJET Program:
F. Paige and S. Protopopescu, BNL Report No. BNL38034, 1986 (Unpublished).

[6] Bicron Corporation, 12345 Kinsman Road, Newbury, OH, 44065-9677, USA. Tel. +1 (216) 564-2251.

[7] Kuraray Intl., 200 Park Ave, New York, NY 10166, USA. Tel. +1 (212) 986-2230.

[8] A. Pla-Dalmau, G.W. Foster and G. Zhang, *Final Results from the SDC Dopant Search for New Green Wavelength Shifting (WLS) Fibers: Volume I*, FERMILAB-TM-1873, December 1993.

[9] Bicron brochure, untitled, contains an overview of the company's capabilities.

[10] A. Bross, Kim Blackman (Bicron Corp.), private communication.

[11] A. Pla-Dalmau, G.W. Foster and G. Zhang, *Summary of the Radiation Damage Studies of the SDC Dopants in Polystyrene*, FERMILAB-TM-1875, December 1993.

[12] C. Zorn, *Fast Scintillators for High Radiation Levels*, in 'Instrumentation in High Energy Physics', ed. Fabio Sauli, World Scientific, (1992), pp. 218-279.

[13] U. Holm and K. Wick, IEEE Trans. Nucl. Sci., Vol. 36, No. 1, (1989), p 579.

[14] M. Adams et al., Nucl. Instrum. and Meth. A, **366**, 263, (1995).

[15] M. Adams et al., *A New Detector Technique Using Triangular Scintillating Strips to Achieve Precise Position Measurements for Minimum Ionizing Particles*, UM HE 95-18, FERMILAB-Pub-95/285-E, September 1995, to be submitted to Nucl. Instrum. and Meth. A.

[16] A. Pla-Dalmau, G.W. Foster and G. Zhang, Volume 1, FERMILAB-TM-1873, December 1993; A. Pla-Dalmau, G.W. Foster and G. Zhang, FERMILAB-TM-1875, December 1993.

[17] D. Lincoln, F. Hsieh, H. Li, Nucl. Instrum. and Meth. A, **366**, 278, (1995).

[18] K.F. Johnson and H.L. Whitaker, Nuclr. Instrum. and Meth., **A301**, 372, (1991).

[19] A. Bross, A. Pla-Dalmau, private communication.

[20] RDN Manufacturing Co. Inc., 960 Lively Blvd, Wood Dale, IL 60191, USA, +1 (708) 595-4876.

[21] A. Bross et al., *Timing Resolution and Linearity Measurements for a Scintillating Fiber Detector Instrumented with VLPC's*, in preparation, to be submitted to Nucl. Instrum. and Meth. A.

[22] S. Margulies and M. Chung, *Development of a multichannel fiber-to-fiber connector for the DØ upgrade tracker*, in Photoelectronic Detectors, Cameras, and Systems, eds. C.B. Johnson and E.J. Fenyves, Proc. SPIE 2551, pp. 10-16, 1995.

[23] M. Chung and S. Margulies, *Development of a multichannel fiber-to-fiber optical connector for the DØ upgrade tracker*, Conference Record, 1995 IEEE Nuclear Science Symposium, 1995 (in press).

[24] M. Born, M. Chung, and S. Margulies, *Test of epoxies for attaching Kuraray multiclad fibers to Delrin*, DØ Note 1776, 29 June 1993.
[25] The diamond fly-cut tool for connectors was designed and made at the Physics Department, Fermilab, Batavia, IL 60510. The single-fiber diamond fly-cut tool was made by Avtech, Advanced Technology and Design Inc., 625 Schneider Drive, South Elgin, IL 60177.
[26] Optical grease used was General Electric VISC-600M; Polydimethylsiloxane, product of GE Silicones, General Electric Company, Waterford, NY 12188.
[27] Mineral oil used was Osco Baby Oil, distributed by OscoDrug, Oak Brook, IL 60521.
[28] Index matching films were provided by Masa Mishina, National Laboratory for High Energy Physics, KEK, Japan. The films were produced by Shinetsu Chemical Co., Japan.
[29] Clear ACE Silicone, manufactured for ACE Hardware Corporation, Oak Brook, IL 60521.
[30] S. Margulies and M. Chung, *Fabrication and testing of clear lightguide fiber bundles for the DØ prototype fiber tracker cosmic-ray test*, in Scintillating Fiber Technology and Applications II, ed. E.J. Fenyves, Proc. SPIE 2281, pp. 26-34, 1994.
[31] M. Chung and S. Margulies, *Aging studies on stressed and unstressed scintillating, wave-shifting, and clear fibers*, in Photoelectronic Detectors, Cameras, and Systems, eds. C.B. Johnson and E.J. Fenyves, Proc. SPIE 2551, pp. 2-9, 1995.
[32] The Zippertubing Co., 13000 S. Broadway, Los Angeles, CA 90061.
[33] S. Margulies and M. Chung, *Estimation of Radiation Doses in the D0 Upgrade Scintillating-Fiber Tracker and Central Preshower Counter*, DØnote#2394 (1994).

Detector Variation	Mean (pe/mm) ±2%	RMS (pe/mm) ±2%	# Events	Mean (Photons/mm) ±20%	Relative Response
Optical Glue	6.13	2.31	39965	24.94	133.1 ± 5.7
404B Normal	4.10	1.72	42823	18.74	100.0 ± 3.0
0.050"	4.36	1.85	40787	18.61	99.4 ± 4.5
0.038"	4.51	1.67	42067	17.96	95.8 ± 4.4
404B Heated	4.67	1.74	38792	17.83	95.2 ± 4.5
Y11 350	4.92	1.85	38575	17.62	94.1 ± 4.2
404A Normal	4.67	1.65	38471	17.33	92.5 ± 4.0
0.100"	5.15	2.05	36309	17.14	91.5 ± 4.1
404A Crazed	4.67	1.74	39649	15.86	84.7 ± 4.5
Black Stripe	4.38	1.97	38273	15.51	82.8 ± 3.6
404A Heated	4.51	1.65	35924	15.50	82.7 ± 3.9
404B Crazed	4.05	1.69	37712	14.62	78.0 ± 5.9
BCF-91A	3.85	1.54	42127	13.44	71.7 ± 3.0
Normal Extruded	3.16	1.38	18540	10.79	57.6 ± 2.5
White Extruded	2.98	1.26	21868	10.57	56.4 ± 2.5
Clear Extruded	2.10	0.96	16643	8.13	43.4 ± 3.1
Black Extruded	0.28	0.28	16198	0.85	4.5 ± 0.2
3HF	0.00	0.00	39317	0.00	0.0 ± 0.0

TABLE IV. Tabulated are the responses of each detector variation in units of photoelectrons (and photons) per millimeter. While the results change if the most probable value is used rather than the mean (most probable $\sim 90\%$ of the mean), the relative response does not. The relative response compares the number of photons exiting each detector variant. Only data in the region of maximum light yield are used (i.e. $|\Delta x| < 0.05$ cm and $|\Delta x| > 0.15$ cm are excluded, where Δx is the distance between the center of the strip and the track intercept at the strip, halfway between the top and bottom surfaces).

Detector Variation	Yield (pe/mm)
350 Unsilvered	2.54 ± 0.05
91A Unsilvered	1.74 ± 0.03
250 Unsilvered	2.17 ± 0.08
404 Heated	4.01 ± 0.06
404 0.038"	3.67 ± 0.05
404B Heated	3.74 ± 0.10
404A Normal	3.28 ± 0.09
404 0.100"	3.89 ± 0.16
404 0.050"	3.92 ± 0.08
404 0.015"	3.67 ± 0.10
404 0.006"	3.97 ± 0.08
404 Normal	3.88 ± 0.13
404B Normal	3.75 ± 0.13
404B Painted	4.25 ± 0.13
404B 1 Black	3.47 ± 0.14
404B 2 Black	3.47 ± 0.08

TABLE V. The yield column shows raw average yield, before corrections for effective quantum efficiency. The error quoted contains both statistical and systematic effects.

Detector Type	Number of Samples	Expected Crosstalk (%)	Average Crosstalk (%)	RMS Crosstalk (%)	Standard Error Crosstalk (%)
0.008"	108	4.51	14.85	2.08	0.20
0.015"	14	8.47	20.17	1.29	0.35
0.006"	14	3.39	10.36	2.09	0.56
Painted	14	4.51	6.06	1.52	0.41
1 Black	10	—	9.93	1.64	0.52
2 Black	14	—	6.06	2.08	0.56

TABLE VI. Detector variants with similar crosstalk characteristics are grouped together. The "type" column is described in more detail in Ref. [15], but the (0.008", 0.015", and 0.006") correspond to the amount of scintillator left below the separation groove. **Painted** corresponds to a variant where the sawtoothed side of a module was painted with white acrylic paint and the **1 Black** and **2 Black** types correspond to the number of black stripes drawn in the area of the separation groove. When the amount of scintillator remaining below the fiber groove is not specifically stated, it can be assumed to be 0.008". Crosstalk fractions k both into the next higher numbered and next lower numbered strips are calculated and the measured mean, RMS and standard error for each crosstalk variant are reported here. When a model exists, the expected crosstalk is given. In all cases, the actual crosstalk exceeds expectations.

Strip Type	Inner Radius	Base	Height	Length	Stereo Angle	# Cells/Octant
Axial	719.55	7.052	5.5	2500	0°	160
Inner Stereo	729.55	7.052	5.5	2703	22.37°	150
Outer Stereo	739.55	7.052	5.5	2740	24.18°	150

TABLE VII. Tabulated are the critical strip dimensions for the design choice where all strips have the same strip cross section. Length dimensions are in millimeters.

Strip Type	Inner Radius	Base	Height	Length	Stereo Angle	# Cells/Octant
Axial	719.55	7.052	5.5	2500	0°	160
Inner Stereo	729.55	6.594	5.5	2711	22.73°	160
Outer Stereo	739.55	6.671	5.5	2716	23.02°	160

TABLE VIII. Tabulated are the critical strip dimensions for the design choice where all octants have aligned edges. Length dimensions are in millimeters.

Assembly and preliminary test	3 hours
Gluing all 8 16-channel connectors	2 hours
Facing the connectors	1 hour
Final test for continuity and light transmission	1 hour
Final assembly with light-tight strain reliefs and Zippertubing	2 hours
Handling and transportation	2 hours
Total	11 hours